



Development and validation of a hybrid data-driven model-based wake steering controller and its application at a utility-scale wind plant

Peter Bachant, Peter Ireland, Brian Burrows, Chi Qiao, James Duncan, Danian Zheng, and Mohit Dua

WindESCo, Inc., 265 Franklin St, Boston, MA 02110, USA

Correspondence: Peter Bachant (pete@windesco.com)

Received: 21 December 2023 – Discussion started: 3 January 2024

Revised: 28 April 2024 – Accepted: 1 October 2024 – Published: 27 November 2024

Abstract. Despite the promise of wind farm control through wake steering to reduce wake losses, the deployment of the technology to wind plants has historically been limited to small and simple demonstrations. In this study, we develop a wake steering control system and deploy it to 10 turbines within a complex 58-turbine wind plant. A multi-month data collection campaign was used to develop a closed-loop tuning and validation process for the eventual deployment of the system to 165 turbines on this and two neighboring wind plants. The system employs a novel actuation strategy, using absolute nacelle position control instead of yaw sensor offsets, along with a model in the loop performing real-time prediction and optimization. The novel model architecture, which employs data-driven input estimation and calibration of an engineering wake model along with a neural-network-based output correction, is examined in a validation framework that tests predictive capabilities in both a dynamic (i.e., time series) and an aggregate sense. It is demonstrated that model accuracy can be significantly increased through this architecture, which will facilitate effective wake steering control in plant layouts and atmospheric conditions whose complexities are difficult to resolve using an engineering wake model alone.

1 Introduction

Wind turbines extract kinetic energy and momentum from the atmosphere to convert them into electrical energy. This process generates a wake downstream of each turbine, where the wind speed is slower and more turbulent than the inflow. As wind turbines are commonly deployed in clusters or arrays, the wake of one turbine can negatively impact the production of neighboring downstream turbines. Wind plant wake losses are site-specific, depending on both the wind climatology (e.g., wind speed, direction, turbulence) and the wind plant layout (e.g., turbine row spacing). Wake losses for US wind plants, both onshore and offshore, have been estimated to be between 2 % and 20 % (Bensason et al., 2021; Lee and Fields, 2021), with offshore wake losses expected to be considerably higher than onshore losses (Rosencrans et al., 2024).

Modern concepts to enable wind farm flow control, where turbines in a wind plant work collectively to maximize over-

all wind plant production, as opposed to “greedy” individual turbine-centric control behavior, have opened up avenues for wake loss mitigation. Recovering as little as 1 % in annual energy production (AEP) through wake mitigation can provide of the order of an additional billion dollars in annual revenue (assuming 1 TWh yr⁻¹ production at USD 0.10 per kilowatt hour; EIA) for an industry that is increasingly subject to margin pressure. Because of this immense opportunity, methods for wake mitigation have recently received significant research attention (Dong et al., 2022; Andersson et al., 2021).

One promising method for wake mitigation is wake steering, which involves strategic yaw misalignment to redirect turbine wakes away from neighboring downstream turbines (Howland et al., 2022b; Campagnolo et al., 2022; Doekemeijer et al., 2021; Campagnolo et al., 2020; van den Broek et al., 2022; Gebraad et al., 2016). Although inducing yaw misalignment for wake steering will reduce the steering turbine’s power, the downstream turbine will experience less wake

overlap and therefore a higher rotor-averaged wind speed, resulting in a net increase in power production for the turbine pair. The effectiveness and viability of wake steering have been demonstrated in simulations (Gebraad et al., 2016; Howland et al., 2022a; Howland, 2021; Debusscher et al., 2022), wind tunnel tests (Campagnolo et al., 2020), and field campaigns (Doekemeijer et al., 2021; Howland et al., 2022b; Ahmad et al., 2019). However, tests within utility-scale wind plants have thus far been relatively simple, primarily being applied to a small number of turbines and in limited wind conditions or using simple control algorithms and actuation techniques, e.g., low-dimensional yaw misalignment lookup tables (LUTs) or static offsets applied to wind vane signals. Thus, wind farm control via wake steering remains relatively immature and has not achieved widespread commercial adoption.

More sophisticated, model-based controllers have been tested in simulations and simple experiments and show promise. The engineering wake models (EWMs) these controllers use have the ability to incorporate more dimensions than just wind speed and direction, e.g., turbulence intensity (TI), turbine state, derating, wind shear, and wind veer, while remaining sufficiently computationally efficient to be used in real time. “Closed-loop” models also incorporate mechanisms for ongoing tuning to better match observations, thereby enabling more effective wind farm control (Doekemeijer et al., 2020; Howland et al., 2022a), which is important since EWMs omit some physics to remain computationally feasible. Howland et al. (2022a) in particular showed how a simple LUT-based controller would fail to optimize plant power in all wind condition regimes.

In this study we develop a model-based wake steering controller with a novel hybrid architecture. The model therein uses data-driven input estimation and calibration of an EWM, along with a neural-network-based “output corrector”. One key feature of this model architecture is that its complexity can be incrementally increased over time, enabling immediate deployment but allowing for continual improvement as operational data are collected, hence closing the loop. We deploy a minimally tuned version of this controller to 10 turbines within a 58-turbine utility-scale wind farm, omitting the output corrector in order to collect a validation dataset for model training and to demonstrate the viability of this hybrid approach in closing the loop and improving model predictive capability – and therefore optimizing performance – over time.

2 Methods

The primary objective of this study was to develop and deploy a wake steering control system that could be applied to wind plants of 50 or more turbines in potentially complex layouts, with varying numbers of online turbines, power limits, and atmospheric conditions, as would be encountered

in the real world. The control problem can be thought of as seeking to maximize the sum of all turbines’ power production, which is a function of the wind characteristics (speed, direction, TI, etc.) and turbine states (online status, power limit, nacelle direction, or yaw angle), the latter of which is the only means of actuation.

Although instantaneous farm power is straightforward to observe through the supervisory control and data acquisition (SCADA) system, there is currently no analytical form available to compute optimal nacelle directions for real-time wake steering control. Despite being shown to be effective in wind tunnel experiments at constant wind direction (Kumar et al., 2023), an extremum-seeking controller would be impractical for the current application given the large number of actuation variables, the variability of wind direction, the relatively long advection times due to the 13D spacing, and the difficulty “dithering” the turbines’ yaw position. A LUT-based controller would require many dimensions to capture all the various permutations of wind conditions and turbine states and would therefore require a prohibitive number of simulations or experiments to develop. For the commercial wind plant studied here, described in Sect. 2.2, a LUT-based controller that allows for variation in wind speed and direction across the plant would contain of the order of 100 billion rows. Thus, a model-based controller was chosen for the present work.

2.1 System architecture

The high-level system architecture of the control system is shown in Fig. 1. In this system, a centralized controller is connected to the SCADA system collecting signals (real power, turbine state, rotor speed, etc.) at a nominal 1 Hz frequency from all turbines (Post et al., 2022). The controller is connected to WindESCo Swarm Edge devices installed in each turbine to be actuated and sends absolute nacelle position set points rather than yaw offsets to the turbines, which allows the control problem to be solved in the global coordinate system instead of being relative to the local wind measurement (Post et al., 2023). This alleviates any issues with yaw measurement nonlinearity (i.e., the measured yaw error at the wind sensor is distorted when the turbine is yawed) and helps the system account for local variation or biases in wind characteristics. In contrast, a non-global control algorithm would make decisions based on a yawing turbine’s local wind direction, but the wind direction could be slightly different at a downstream turbine, causing suboptimal set point selection. Every minute, an optimization algorithm uses the wake model to predict farm power as a function of yaw to determine the optimum values, and corresponding nacelle position set points are subsequently sent to the Swarm Edge devices.

Digging one level deeper, the wake model architecture is shown in Fig. 2. This model is split into three parts:

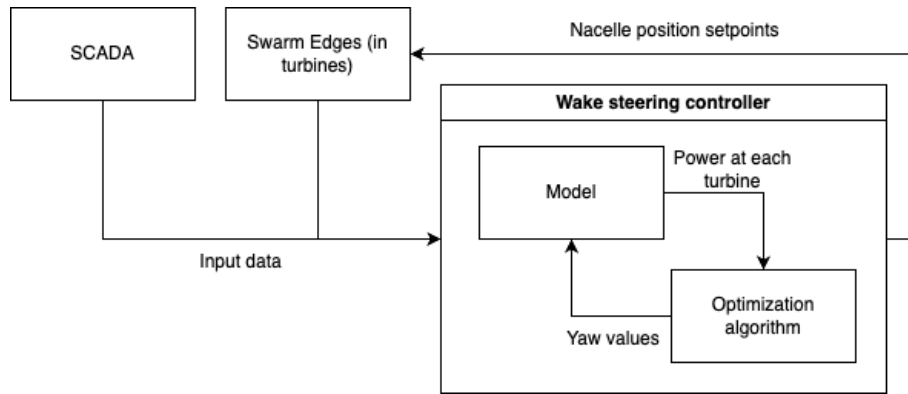


Figure 1. Wake steering controller system architecture.

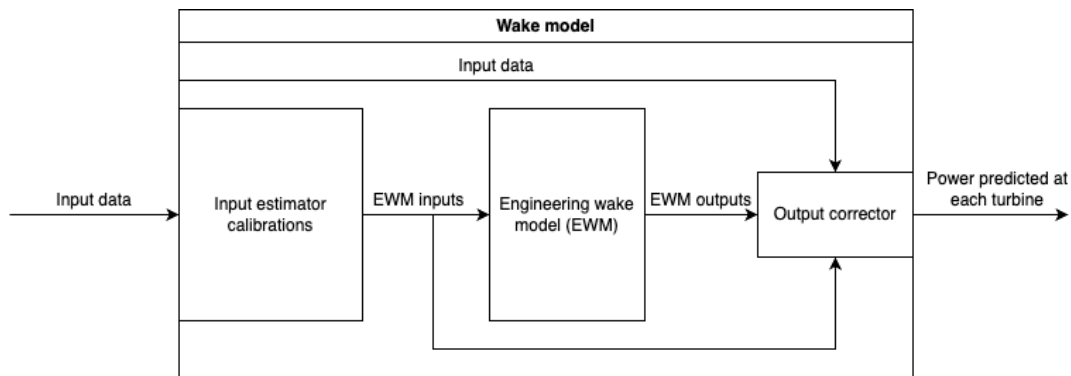


Figure 2. Wake model architecture.

1. calibrated input estimation
2. a physics-based EWM
3. neural-network-based output correction.

In the input estimation step, raw data collected from the plant are transformed into input values suitable for the steady-state EWM. The input calibrations use relatively simple models, some of which can be derived from historical data in which wake steering was not active, but these calibration models are critical to getting accurate predictions from the EWM, as seen later. Lastly, all input data, EWM inputs, and EWM outputs are sent to the output corrector, which has the job of making up for any physics not captured in the EWM. The input estimation and output correction parameters are intended to be solved for in an automated offline process, after which the controller is updated approximately daily. This is in contrast to other closed-loop algorithms, which might update their parameters every iteration.

2.2 Pilot installation and data collection campaign

A preliminary version of this wake steering control system was deployed to a commercial onshore wind farm in Utah,

USA. The initial deployment did not use an output corrector, as the primary goal was to collect data where wake steering was attempted by a minimally tuned model to develop the full closed-loop model training and validation process.

The wind farm layout is shown in Fig. 3. This site consists of 58 Clipper C99 model turbines, each with a hub height of 80 m, a rotor diameter (D) of 99 m, and a rated power of 2.5 MW. The transverse spacing between turbines is approximately $2.8 D$, while the downstream turbine row spacing is about $13 D$. For the pilot deployment, 10 out of the 58 turbines were augmented with hardware and software to enable wake steering control, with the assumption that the remaining turbines (including turbines at two adjacent co-operated sites, 165 turbines in total) would eventually be instrumented and controlled. To the best of our knowledge, this is the largest campaign of its kind, with the next largest campaign being that of Howland et al. (2019), where six utility-scale turbines were wake steered. Further, this is the first wake steering control system deployed that uses absolute nacelle position set points sent from a centralized controller.

Waking occurs at a variety of wind directions, but the predominant waking wind direction is from the south and south-southwest, as demonstrated by the wind rose in Fig. 4. For this reason, and because two co-operated wind farms situ-

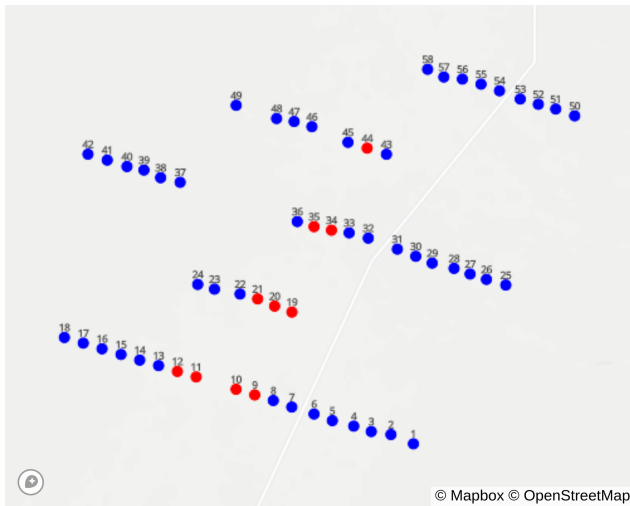


Figure 3. The distribution of wind turbines (colored circles) at the wind farm studied here. The red circles indicate turbines with Swarm Edge hardware and software. The turbine IDs are labeled to aid future discussions.

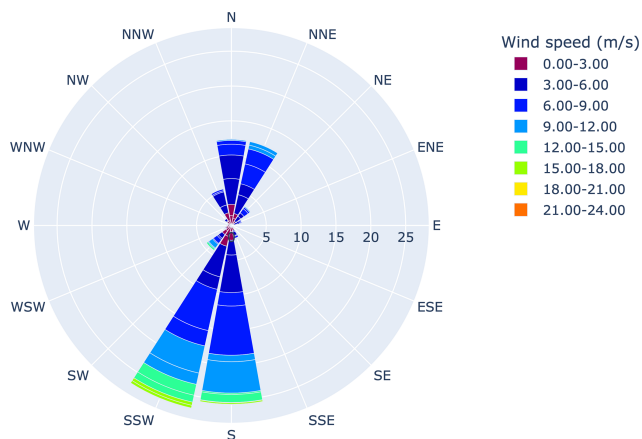


Figure 4. The wind rose for the 3 years prior to the start of the pilot test (September 2018–September 2021).

ated immediately north of the site can cause wind farm waking under northerly wind conditions, we direct our attention to southerly winds in this study. The farm layout presents a challenge for wake steering control given its relatively long spacing in the predominant wind direction and close spacing in the transverse wind direction, meaning that flow control will need to occur over relatively long distances and with relatively high precision to avoid steering wakes into turbines instead of away from them. This larger distance might also mean lower wake losses since there is more room for wake spreading and recovery. As shown later, wake losses are approximately 17% when second-row turbines are directly waked, thanks to significant time spent in stable atmospheric conditions.

It should be noted that at this spacing a downstream rotor's half width represents an angle of approximately 2° , meaning that a small shift in wind direction can produce a large change in the location of the wake and therefore its impact on a downstream turbine. It therefore follows that a controller will need a highly accurate estimate of wind direction to determine optimal yaw offsets.

The pilot wake steering data collection campaign took place over 4 months, from 1 December 2021 to 1 April 2022. During this time, we gathered data with wake steering toggled on and off every hour to attempt to collect equal amounts of data in each state in similar wind conditions. A preliminary minimally tuned wake model was deployed on the farm during this measurement campaign. As seen in Sect. 3.1, while this model did not predict farm power with acceptable accuracy, and therefore likely did not achieve optimal wake steering performance, it did show evidence of power gains at downstream turbines when wake steering. More importantly, this pilot data collection phase allowed us to naturally collect training data in a wide range of wind conditions and for various wake steering scenarios, enabling the closed-loop model training and validation process to produce a model that should achieve optimal wake steering performance going forward.

2.3 Engineering wake model

NREL's FLOW Redirection and Induction in Steady State (FLORIS) EWM (version 2.4) was selected for the current work (NREL, 2021) due to its prevalence within the wind energy community (e.g., van Beek et al., 2021; Meyers et al., 2022), its applicability to wind farm control, and its computational speed and simplicity. FLORIS predicts the steady-state flow field in a wind farm, including the power of each turbine, given the ambient wind conditions as well as the wind turbine and wind plant configuration information. Typical FLORIS model wind inputs include the ambient wind direction, ambient wind speed, ambient TI, wind shear, and wind veer. Other FLORIS model wind farm inputs include each turbine's geometric information (hub height, rotor diameter, spatial coordinates) and performance characteristics (power curve, thrust curves, and typical power losses under off-yawed conditions).

FLORIS does have a wide range of sub-models to select from, each with their own tuning parameters, e.g., to control how fast wakes recover or deflect when steering. The default sub-models and parameters have typically been determined through a combination of theory, experiments, and high-fidelity simulations (Doekemeijer et al., 2020; Bastankhah and Porté-Agel, 2016). Since this study is focused on estimating ambient conditions and using machine learning models, we used FLORIS with its default wake models and parameters, which are described in detail in NREL (2021). These included the Crespo–Hernandez wake turbulence model (Crespo and Hernandez, 1996), the

sum of squares freestream superposition wake combination model, the Gauss deflection model (Bastankhah and Porté-Agel, 2016; King et al., 2021), and the Gauss–legacy velocity model (Bastankhah and Porté-Agel, 2016; Niayifar and Porté-Agel, 2016).

2.4 Input estimation and calibration

We now discuss the approach for preprocessing data to estimate the input conditions passed to the EWM, along with the model state (i.e., calibrations), in order to produce the most accurate power predictions possible.

2.4.1 Turbine performance curves

To predict turbine power output, FLORIS computes the flow field velocity and then uses the nondimensional power coefficient (C_P) to determine the power at each turbine. C_P is defined as

$$C_P = \frac{P}{\frac{1}{2}\rho AU_\infty^3}, \quad (1)$$

where P is the power produced by the turbine, ρ is the air density, A is the rotor-swept area, and U_∞ is the ambient wind speed.

We consider two possible approaches for determining the power coefficient curves:

1. Use the values as published by the original equipment manufacturer (OEM). This approach was used in our initial deployment.
2. Infer the power coefficient curves from historical SCADA data.

Although the curves derived using both methods should be similar, it is common for them to differ due to differences between the idealized turbine performance assumed by the OEM and its actual performance on site or due to changes in nacelle transfer functions. Since we know our wind speed estimation algorithm will use nacelle wind speed, it makes sense then to compute the C_P curves as a function of the nacelle wind speed. Doing so will implicitly include nacelle transfer function effects on the measured wind speed, removing this potential source of bias when mapping wind speed to power. Note that with this approach it is possible to compute unrealistic power coefficients, i.e., those above the Betz limit, as a result of inaccurate nacelle transfer functions. However, since FLORIS only uses the C_P curve to compute power after computing wind speed, the resulting power predictions should overall be consistent with the power curve as computed against nacelle anemometer measurements and, therefore, with observed SCADA data.

Figure 5 compares the OEM C_P curve with one modeled using 3 years of historical SCADA data; differences between the two curves are most evident in the 5 to 12 m s⁻¹ range.

Turbines that were waked, offline, or derated were removed from the dataset, as were turbines whose nacelle wind speed was below the OEM cut-in wind speed. The last filtering step was added to avoid biased C_P estimates at low wind speeds, as turbine power is often strongly affected by the rotor inertia. While it is also possible to determine turbine-specific C_P curves using historical SCADA data, this approach resulted in noisy results (particularly for turbines undergoing frequent maintenance or derating). Hence, a single C_P curve was derived and applied to all turbines since all turbines on the farm were of the same model. While assuming a single C_P wind speed curve may lead to biases in the model power predictions in some scenarios (e.g., if measurement biases differ between individual turbines), this was not observed to be a significant issue on this particular wind farm.

FLORIS also requires thrust coefficient (C_T) curves, which govern momentum extraction and affect wake deficits. The thrust coefficient C_T is defined as

$$C_T = \frac{T}{\frac{1}{2}\rho AU_\infty^2}, \quad (2)$$

where T is the thrust produced by the turbine. Unlike the C_P curves, there is no independent way to verify the C_T curves. Therefore, the values defined by the OEM were used, which relies on the assumption that the wind speeds in the thrust coefficient values match those from the nacelle anemometers.

2.4.2 Power loss due to yaw misalignment

The power of a turbine will decrease under non-zero yaw angles. Capturing the proper relationship between yawing and power loss is important due to its influence on wake steering optimization. This relationship is typically modeled through a cosine exponent p ,

$$P = P_0 \cos^p \gamma, \quad (3)$$

where P is the power produced by a turbine with a yaw error of γ , and P_0 is the power that would be produced at 0° yaw error.

The FLORIS default value of p is 1.88, which is based on large-eddy simulation (LES) results (Gebraad et al., 2016). (To model power production properly above rated wind speeds, FLORIS adjusts the turbine's effective wind speed rather than the power using a cosine exponent of $p/3$. This effective wind speed is then used to look up the power.) Subsequent studies have shown that p may vary across different turbines and wind conditions (Howland et al., 2020; Liew et al., 2020). However, we did not observe a significant difference in model performance when using the default value of p versus values obtained through a separate estimation procedure based on SCADA data. Therefore, the FLORIS default p value of 1.88 was used in this study. Although we use the

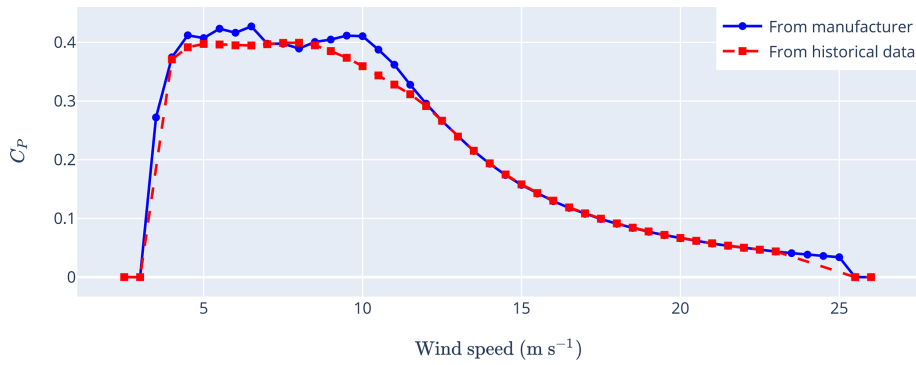


Figure 5. The C_p curve from the OEM and derived from historical SCADA data. Note that there is a minor discrepancy at 6.5 m s^{-1} in the OEM curve, where our transcription was 553 kW instead of the OEM’s 533 kW .

default cosine exponent, the power loss with yawing relationship will be implicitly accounted for in our output corrector model discussed later.

2.4.3 Ambient wind speed estimation

One required input to the FLORIS wake model is the ambient wind speed. First, we apply a rolling average in time on the high-frequency wind speed measurements; i.e.,

$$\bar{U}_i(t) \equiv \frac{1}{T_U} \int_{t-T_U}^t U_i(t') dt', \tag{4}$$

where $\bar{U}_i(t)$ is the time-filtered velocity of turbine i at time t , $U_i(t)$ is the high-frequency velocity of turbine i at time t , and T_U is the size of the averaging window (the subscript U indicates that it applies to the velocity). We found model performance to be generally equivalent for time filters between 1 and 10 min and therefore used a constant value of $T_U = 5 \text{ min}$ in this study.

We next need to determine which of these turbine velocities correspond to unwaked turbines, since the wind speed inputs to our waked model correspond to ambient wind conditions. We estimate which turbines are unwaked based on the estimated ambient wind direction computed in Sect. 2.4.4 and the geometric parameterization in IEC (2017) (see Fig. A1 of this reference). From our experimental data, we observed that under periods of high atmospheric stability, wakes can persist for longer distances than the 20 rotor diameter cutoff assumed in IEC (2017), and therefore we require a turbine to be at least 30 rotor diameters downstream of a potential waking turbine to be considered unwaked.

Since wind speeds measured at operational and non-operational turbines may be different (e.g., nacelle anemometer wind speeds are affected by rotor-induced flows and nacelle transfer functions) and the C_p curve in Sect. 2.4.1 was derived only from operational turbines, it is recommended to exclude wind speed measurements from

non-operational turbines. This can be done by excluding turbines whose power or rotor speed falls below some threshold. However, even after these filtering steps, it is possible that a turbine will exhibit implausible nacelle anemometer wind speed measurements. These can be excluded by filtering any turbine wind speeds that are a certain number of standard deviations from the mean value over all turbines, though this treatment was not found to be necessary for wind speed in the current study.

We finally apply a spatial filtering step to translate turbine-level time-filtered wind speed measurements to wind speed inputs in our wake model. That is, for turbine i , we compute the ambient, spatially averaged wind speed $U_{\infty,i}(t)$ as

$$U_{\infty,i}(t) \equiv \frac{\sum_j w(\mathbf{x}_i, \mathbf{x}_j) \bar{U}_j(t)}{\sum_j w(\mathbf{x}_i, \mathbf{x}_j)}, \tag{5}$$

where the summation \sum_j takes place over all turbines (excluding those removed from the analysis due to waking, offline states, or implausible data), with weights between turbines i and j with Cartesian positions of \mathbf{x}_i and \mathbf{x}_j defined as

$$w(\mathbf{x}_i, \mathbf{x}_j) \equiv \frac{\exp(-r^2/2)}{\sqrt{2\pi}}, \tag{6}$$

where

$$r \equiv \frac{\|\mathbf{x}_i - \mathbf{x}_j\|/D}{\mathcal{N}_U}. \tag{7}$$

D denotes the turbine rotor diameter, and \mathcal{N}_U is a nondimensional scaling factor corresponding to the number of rotor diameters to use in the spatial filter. Small values of \mathcal{N}_U allow for a larger degree of wind speed heterogeneity or non-uniformity in the model, whereas high values of \mathcal{N}_U correspond to a more homogeneous wind speed field.

$\mathcal{N}_U \rightarrow \infty$ is equivalent to a farm-wide average wind speed, which is the most common approach in the literature (Doekemeijer et al., 2020; Howland et al., 2022b). For

large farms, however, it may be important to capture spatial wind speed variations to accurately predict power levels. Doekemeijer et al. (2022) observed heterogeneous wind speeds on the industrial-scale wind farms in their study but also noted difficulties in accurately modeling these heterogeneous wind speeds with FLORIS due to either deficiencies in the FLORIS model or uncertainties in the background wind conditions. They derived a generalized inflow profile from annual wind speed measurements and used this profile to translate a homogeneous farm-averaged wind speed into heterogeneous turbine-level wind speeds. The advantage of our approach over that of Doekemeijer et al. (2022) is that it can account for more instantaneous spatial variability in the wind speed on a farm. We assess the effect of including wind speed heterogeneity in our model in Sect. 3.

2.4.4 Ambient wind direction estimation

The approach for ambient wind direction estimation mirrors much of that for ambient wind speed estimation but with an additional complexity associated with the use circular quantities.

As before, we start by applying a time filter to $\theta_i(t)$, the high-frequency wind direction signal for turbine i :

$$\bar{\theta}_i(t) \equiv \text{atan2} \left(\frac{1}{T_\theta} \int_{t-T_\theta}^t \sin \theta_i(t') dt', \frac{1}{T_\theta} \int_{t-T_\theta}^t \cos \theta_i(t') dt' \right), \quad (8)$$

where atan2 is the two-argument arctangent function, and T_θ is the wind direction temporal filter width. (As with the wind speed (Sect. 2.4.3), we observed little dependence on this parameter for T_θ between 1 and 10 min and therefore used a constant value of $T_\theta = 5$ min.) Outlier filtering is then applied to $\bar{\theta}_i(t)$ to exclude offline turbines and turbines whose estimated wind directions differ significantly from the mean wind direction (in a circular sense) across the farm.

At this stage, as with the wind speeds, we apply a spatial filtering process (with nondimensional wind direction filter width \mathcal{N}_θ , analogous to wind direction filter width \mathcal{N}_U from Sect. 2.4.3) to obtain the spatially and temporally filtered ambient wind direction $\theta_{\infty,i}(t)$. For estimating wind direction, the nearly universal approach in the literature (Fleming et al., 2017; Ahmad et al., 2019; Howland et al., 2019; Fleming et al., 2020; Simley et al., 2021; Doekemeijer et al., 2021, 2022) is to use a single wind direction (corresponding to $\mathcal{N}_\theta \rightarrow \infty$). However, in our initial pilot study (Sect. 2.2), we used $\mathcal{N}_\theta = 5$ to attempt to model wind direction heterogeneity on the farm. We determined, however, that this did not improve the model performance on this farm, presumably due to difficulties in FLORIS of accurately modeling heterogeneous wind directions. For that reason, we switched to a simple farm average for the wind direction in the remaining models studied in this paper (see Sect. 3.2). We denote this farm-averaged wind direction as $\theta_\infty(t)$.

When computing the wind directions, there are two potential sources of the high-frequency wind direction $\theta_i(t)$. The simplest is the SCADA wind direction signal; however, this signal is often not calibrated to true north, and even after calibration, it may not be sufficiently accurate for use in wake steering. We also have access to the nacelle direction reported by GNSS (global navigation satellite system) compasses in the Swarm Edge devices installed on 10 turbines. The wind direction can be computed from the GNSS compass nacelle direction and the measured yaw error, and we expect this measure of wind direction to provide a higher level of accuracy. In our initial “naive” model deployment, we used a mix of both signals: GNSS compass wind directions were used where available, and SCADA nacelle directions (that were manually calibrated in the past based on direction readings taken by operators in the field) were used otherwise. However, this approach gave unrealistic wind direction predictions (due to issues calibrating the SCADA wind directions and inconsistencies in the sensors), and so we switched to using only GNSS compass wind directions in all other models, assigning turbines without GNSS compasses zero weight in the spatial filtering process.

The wind direction obtained through this approach, however, may differ from that needed in the model to best capture wakening due to sensor biases, underlying atmospheric conditions, or model inaccuracies. One approach for tuning the wind direction to best capture wakening is to use the input measurements as is but to adjust model coefficients (e.g., those pertaining to veer or wind direction deflection by the rotor). However, this approach is not preferred in the case of sensor biases, since we may be tuning model coefficients to unrealistic values to compensate for inaccurate input conditions. We therefore instead adjust the wind directions themselves following a similar approach to that outlined in Kanev (2020) and Doekemeijer et al. (2022).

Figure 6 shows the target and reference turbines selected for estimating the wind direction adjustments. Target turbines are subjected to wakening from one row of upstream turbines when wind is from the south. Reference turbines are the southernmost turbines, excluding turbines outfitted with Swarm Edge devices to avoid confounding effects on power from high yaw errors. We could extend our analysis to deeper turbine rows to determine offsets for these turbines. However, we observed that the wakening signal became weaker and more diffuse for these turbines, making parameter estimation difficult. A similar conclusion was reached in Kanev (2020).

For each target turbine i , we compute the power ratio at time t , $R_i(t)$, as

$$R_i(t) = \frac{P_i(t)}{\frac{1}{N_{\text{ref}}} \sum_r P_r(t)}, \quad (9)$$

where $P_i(t)$ is the power produced by turbine i at time t , N_{ref} denotes the number of reference turbines selected, and \sum_r indicates a summation over each reference turbine. Fol-

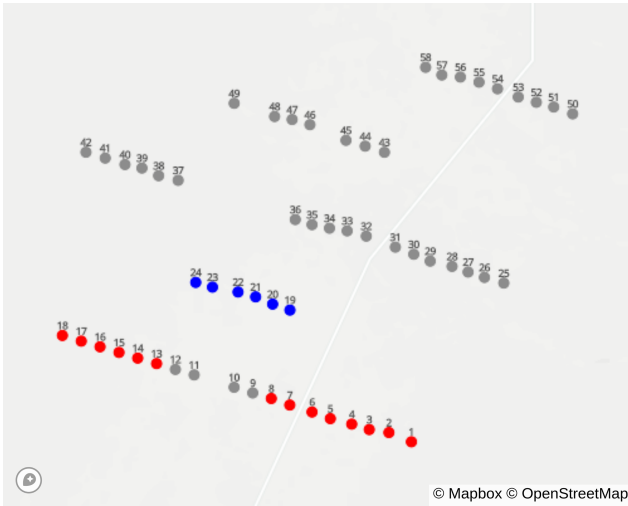


Figure 6. Turbines selected as targets (blue) and references (red) for estimating wind direction offsets.

lowing the typical convention in the literature (Kanev, 2020; Fleming et al., 2020; Doekemeijer et al., 2022), these temporal results are then binned by the farm-averaged ambient wind direction $\theta_\infty(t)$, and the mean power ratio in each bin is reported. Results are computed over 4 months of operational data using a 5 min temporal averaging period. Prior to binning, we filter target and reference turbines for yaw errors below 5° (to avoid power losses due to yawing), region 2 wind and power conditions, and wind directions between 152 and 242° (measured clockwise, with 0° indicating true north to ensure wind is from the south).

For a given wind direction bin, we compute the model predictions of the power ratio as a function of wind direction by running FLORIS with a single wind direction (corresponding to the center of the bin), a single wind speed (corresponding to the overall mean wind speed in the dataset), and a TI of 10%. While we could obtain more representative model results by simulating each of the wind directions, wind speeds, and turbulence intensities in our observations, the primary focus of our analysis at this stage is on matching the directional pattern of waking and unwaking in the data, for which a fixed wind speed and TI are sufficient and computationally advantageous.

Following Doekemeijer et al. (2022), we determine the optimal offset to the wind direction $\Delta\theta_i$ at each turbine to maximize the correlation between the binned power ratios in the observations $R_i(\theta_\infty)$ and those from the model $R_i^{\text{model}}(\theta_\infty)$:

$$\Delta\theta_i \equiv \arg_{\Delta\theta_i} \max \left(r \left[R_i(\theta), R_i^{\text{model}}(\theta + \Delta\theta_i) \right] \right). \quad (10)$$

Here, r is the Pearson correlation coefficient. We selected the correlation coefficient as our optimization function rather than a quantity like the mean-squared error because our model has not yet been tuned to match the waking strength observed in the data. At this stage, we simply want to ensure

we can match the directional pattern of waking and unwaking.

Figure 7 shows the correlation coefficients for each of the six target turbines identified in Fig. 6. Wind direction offsets ranging from -10 to 10° are used under the assumption that the wind direction shift in excess of 10° is not needed. (Negative values indicate a counterclockwise correction to the wake direction, whereas positive values indicate a clockwise correction.) If no wind direction offsets were needed, the correlation coefficients should peak at $\Delta\theta_i = 0^\circ$. The fact that the peak is offset from 0° indicates that this additional adjustment to the wind direction signal is necessary. For many of the turbines, we observe two nearly identical peaks: one near -7° and one near $+5^\circ$. This pattern makes sense geometrically: because of the close row-wise spacing of the front-row turbines, many of the target turbines (19, 20, 23, 24) can be waked by a different front-row turbine as a result of a 12° (-7 to $+5^\circ$) wind direction shift.

The challenge is then in determining whether a turbine should have a positive or a negative wind direction shift. To resolve this, we consider turbine 22. Because there is a gap in the front-row turbines upstream of turbine 22 (see Fig. 6), we do not expect the same symmetrical pattern in the correlation coefficients. Indeed, we notice that turbine 22 exhibits a peak for $\Delta\theta_i = 5^\circ$ but no corresponding peak for negative $\Delta\theta_i$. Figure 8 compares the mean power ratio in the data to that predicted by the model under a $+5^\circ$ wind direction shift. The agreement in trends between the data and model is good, showing limited waking (power ratios near 1) for wind directions around 190° (corresponding to the gap in the front-row turbines) and waking (power ratios near 0.8) around 180 and 200° .

Based on this analysis, we assign a positive wind direction offset of 5° for turbine 22 and assume the positive solution branch also holds for the remaining turbines. Since most target turbines show a peak at $+5^\circ$ (turbines 20 and 23 are slight exceptions, with peaks at $+6$ and $+4^\circ$, respectively), we apply a single global $+5^\circ$ wind direction offset.

To explore the sensitivity of the wind direction offset to the time range considered, we repeated this analysis over different 2-month training periods within the overall dataset. While there were small variations in the optimal wind direction offsets between different times for certain turbines (typically of the order of $1-2^\circ$), a farm-wide wind direction offset of about 5° was a consistent finding. We therefore use a global, time-invariant offset in wind direction.

2.4.5 Ambient turbulence intensity estimation

The ambient TI computation is performed similarly to the ambient wind speed computation presented in Sect. 2.4.3, with an additional preliminary step of computing the TI $I_i(t)$ from the high-frequency wind speed:

$$I_i(t) \equiv \frac{\sigma U_i(t)}{\langle U_i(t) \rangle}, \quad (11)$$

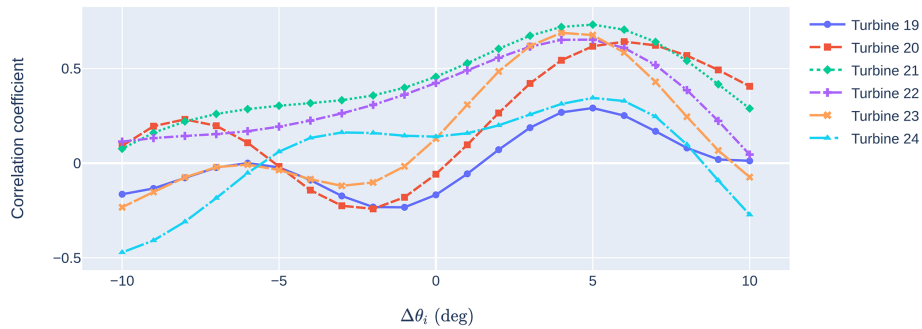


Figure 7. Correlation coefficients computed at various wind direction offsets for each of the target turbines. Turbines are numbered 19–24, corresponding to their identification in Fig. 6.

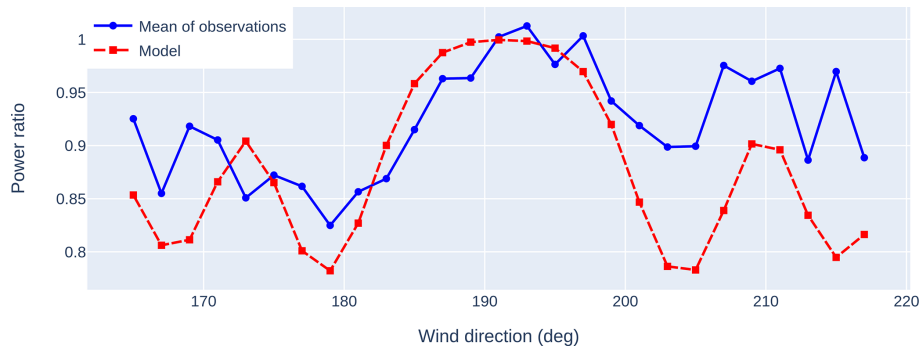


Figure 8. Comparison between model predictions and mean of observations for the power ratio of turbine 22 as a function of wind direction under a +5° wind direction shift in the model.

where $\sigma_{U_i(t)}$ denotes the standard deviation of the high-frequency wind speed for turbine i over the previous 10 min time window, and $\langle U_i(t) \rangle$ is the mean of the high-frequency wind speed of turbine i over the same time window.

The approach then closely parallels the wind direction approach, with removal of TI values from waked turbines and optional outlier filtering. We finally apply a simple spatial average to obtain a single turbulence intensity value $I_\infty(t)$ to use in the model at time t .

The estimate of the ambient TI $I_\infty(t)$ made directly from nacelle anemometry is not necessarily the best input to the FLORIS model. When modeling TI, nacelle anemometers, by virtue of their location downstream of the rotor, are affected by rotor-induced turbulence and so do not capture the ambient flow characteristics (Smith et al., 2002). Wind turbine manufacturers introduce a nacelle transfer function to estimate the ambient wind speed based on measurements behind the rotor; however, the theory, implementation, limitations, and accuracy of a given nacelle transfer function are rarely disclosed. For example, St. Martin et al. (2017) found that different nacelle transfer functions should be used based upon the atmospheric stability and turbulence levels. In addition, even if we had perfect knowledge of the ambient turbulence intensity, this quantity will likely not exactly correspond to the FLORIS model TI, which should be viewed as a

model parameter that influences wake spreading and stability rather than as a perfect correlate of the ambient TI observed in the field.

For these reasons, we considered an additional step to map the ambient TI as measured by the nacelle anemometer (I_∞) to that needed in the FLORIS model (\mathcal{I}_∞) to better resolve the observed waking conditions. To do so, we first select turbines, wind directions, and wind speeds with high levels of waking (as indicated by frequent occurrences of low power ratios) and denote these as waking cases of interest. Historical data corresponding to each waking case of interest are then binned by the ambient nacelle TI. In each nacelle TI bin, we compute the optimal turbulence intensity to use in FLORIS to minimize the mean-squared difference between the power ratio of the turbine in the historical data for a given wind speed and direction, $R_i(I_\infty|U_{\infty,i}, \theta_\infty)$, and that predicted by the model, $R_i^{\text{model}}(\mathcal{I}_\infty|U_{\infty,i}, \theta_\infty)$:

$$\mathcal{I}_\infty(I_\infty) \equiv \arg_{\mathcal{I}_\infty} \min \left(\left[R_i(I_\infty|U_{\infty,i}, \theta_\infty) - R_i^{\text{model}}(\mathcal{I}_\infty|U_{\infty,i}, \theta_\infty) \right]^2 \right). \quad (12)$$

Equation (12) gives optimal FLORIS turbulence intensity values \mathcal{I}_∞ for a range of different nacelle turbulence intensities I_∞ , from which a regression relationship can be formulated.

In the initially deployed model (see Sect. 2.2), we determined the following TI mapping based on a single waking case of interest:

$$\mathcal{I}_\infty = 0.0571 - 1.83I_\infty + 29.6I_\infty^2 - 67.1I_\infty^3. \quad (13)$$

However, we found that while a given mapping tended to improve the power predictions of the turbine under consideration, the results did not generalize to other turbines in the wind farm. The model without a TI mapping gave the most consistent results over the range of turbines considered, and so we chose to omit the TI mapping for the new models developed here. We expect, however, that TI mapping may still be beneficial on other farms, especially those where the nacelle anemometer TI reading differs significantly from the ambient TI.

2.5 Output corrector

The output corrector architecture devised is shown in Fig. 9. Available inputs are the raw, high-frequency input data from the SCADA system and Swarm Edge devices, the EWM inputs, and the EWM outputs. The last block before returning predicted power is a so-called “feature space filter”, which prevents the output corrector from returning its machine learning predictions for feature values (in a multidimensional sense) very far from those upon which it has been trained, falling back to the EWM predictions in these cases. Again, the purpose of the output corrector is to provide the most accurate predictions possible for the power of every turbine on the plant. The output corrector must also be able to handle varying yaw angles for any upstream turbines to be used for optimization.

In general, the measurement system provides signals at turbine i at time t , representing the power, wind speed, air density, yaw misalignment, and nacelle position for the set of m turbines on the farm $i \in 1, \dots, m \equiv \mathcal{T}$. In this setup, we wish to develop a set of models that will predict the power at every turbine within the farm. Waked and freestream turbines are treated differently. The set of freestream turbines is defined as $\mathcal{T}_f \subseteq \mathcal{T}$, and the set of waked turbines is defined as $\mathcal{T}_w \subseteq \mathcal{T}$ such that $\mathcal{T}_w \cap \mathcal{T}_f = \emptyset$. These signals are combined into a feature matrix in the form $\mathbf{X}_{i,s}(t)$, where the subscript i indicates the turbine ID, “s” indicates the signal name, and t indicates the timestamp. The feature matrix can include raw input data, EWM inputs, EWM outputs, and time-lagged versions of each.

We use this feature matrix as the input into an arbitrary machine learning model framework. The aim is to predict the power at each turbine on the farm at a desired frequency, and at least one model will be trained for each target turbine. In this framework, we have mTk possible features in the full dataset, where k is the number of signals collected, and T in this context describes the number of time lags available for use. In our study, we limit T to 2: the current time and the

1 min time lag. Limiting the discussion to the physically relevant signals listed above, including a 1 min time lag of each signal, and excluding the wind speed and power signals of the target turbine, we have 574 features to choose from when predicting the power of a single turbine.

We can treat the power predicted at a single turbine, $\bar{P}_i(t)$, as a function of the data collected by all other turbines on the farm, $\bar{P}_i(t) = f(\mathbf{X}_{i,s}(t))$. However, this level of dependence creates problems for a machine learning model when a turbine is offline, derated, or disconnected from the SCADA server. Automated imputation methods are challenging to deploy due to the uncertainty in the case of a missing or altered signal. One way to combat this problem is through the use of dimensionality reduction tools, which are commonplace in data science applications.

We use a physics-informed dimensionality reduction to select features with causative relationships between control variables and power production. This algorithm is based on a parameterized modification to IEC (2017), which is used to approximately define the wind direction sector where a turbine is waked by another turbine. The width of the waked sector at turbine i and generated by turbine j is defined by

$$\theta_w[i, j] = \arctan(2.5D_e/L_e + 0.15) + 10, \quad (14)$$

where D_e is the equivalent rotor diameter, and L_e is the actual straight-line distance between turbines i and j (IEC, 2017). The wind directions where turbine i is waked by turbine j are then computed as $\theta_{\min}[i, j] = \theta_c[i, j] + \alpha\theta_w/2$ and $\theta_{\max}[i, j] = \theta_c[i, j] - \alpha\theta_w/2$, where $\theta_{\min}[i, j]$ and $\theta_{\max}[i, j]$ are the minimum and maximum wind directions in which turbine i is waked by turbine j . Here, θ_c is the angle between turbines i and j . Our modification to this approach is to use a parameterized scaling factor, α , and a distance threshold parameter, D_{\max} , when computing the wind sector bounds. Here, α controls the final width of the wake sector. D_{\max} is used to discard any waked sectors where $L_e > D_{\max}$. The IEC standard can be recovered using $\alpha = 1$ and $D_{\max} = 20$.

This partitioning algorithm takes the following steps, for each turbine i :

1. Determine the set of turbines that wakes turbine i , \mathcal{T}_u .
2. Determine the bounds of each wake sector $\theta_w[i, j] \forall j \in \mathcal{T}_u$.
3. Merge any overlapping wind sectors, noting which turbines generated the wake in that sector.
4. Find all wind directions where turbine i is not waked by any upstream turbine, and add these to the set of wind sectors.

This algorithm is repeated for each turbine on the farm. It results in a set of wind sectors for each turbine, Θ_i . In each wind sector, we have a set of turbines, $\mathcal{T}_{i,\Theta}$, whose signals are

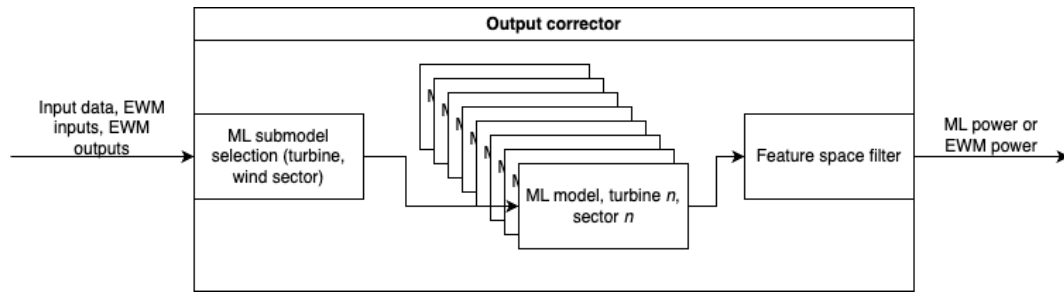


Figure 9. Output corrector architecture.

relevant to predicting the power at turbine i . Subsequently, the model training process is described as follows:

1. For each turbine, i , select the set of wind sectors Θ_i .
2. For each wind sector in Θ_i , select relevant turbine signals, \hat{s} , from all turbines in $\mathcal{T}_{i,\Theta}$.
3. Remove the power and wind speed signals of turbine i from the feature set.
4. Subset the full dataset $X_{i,s}(t)$ to the relevant signals, $X_{i,\hat{s}}(t)$.
5. Find the set of timestamps, \hat{t} , where the farm-averaged wind direction lies in the chosen wind sector.
6. Train the model on $X_{i,\hat{s}}(\hat{t})$.

Thus, a single model is trained for each turbine and each wind sector. The number of wind sectors varies per turbine and depends on the farm layout. The number of features used to train each model depends on the number of waked turbines in the chosen wind sector.

For the remainder of this study, models for turbines in waked sectors use the following features measured at upstream turbines to predict the power of the waked turbine: wind direction as measured by the GNSS compass and nacelle anemometer, 1 min rolling average of SCADA wind speed, 1 min rolling average of estimated yaw error, 10 min rolling TI measured at the nacelle, 1 min rolling average of SCADA power, 1 min rolling average of SCADA power lagged by 1 min, and the EWM-predicted power. In addition, the models use the same features measured at the target turbine but with the target turbine's current 1 min rolling average of wind speed and power measurements omitted (the time-lagged measurements are still used as features).

For the remainder of this study, models for turbines in freestream sectors use the following features measured at the turbine of interest to predict its own power: 1 min rolling average of estimated yaw error, 10 min rolling TI measured at the nacelle, wind direction as measured by the GNSS compass and nacelle anemometer, 1 min rolling average of SCADA wind speed, 1 min rolling average of SCADA power lagged by 1 min, and the EWM-predicted power.

Six features are always used to predict a freestream turbine's power. For a waked turbine, $7n + 5$ features are used, where n is the number of upstream turbines used in the modeling. This results in a minimum of 12 features and a maximum of 404, depending on how the partitioning is done.

The default IEC distance cutoff of 20 rotor diameters was used, and the disturbed wind sector width was reduced by a factor of 8 from the IEC value (IEC, 2017). This was then used to partition the input space with a varied number of features per model. A minimum of 1000 samples were required in each sector before a model was trained. A multilayer perceptron was trained for each turbine–wind sector with hidden layers of (20, 50, 50, 50, 50, and 20) nodes and a rectified linear unit (ReLU) activation function. Scikit-learn's `MLPRegressor` implementation (Pedregosa et al., 2011) was used in this study.

ReLU functions are piecewise continuous and not differentiable, which can be challenging for gradient-based optimization of farm power. Differentiable activation functions are available in other machine learning libraries, e.g., TensorFlow, though these significantly increase the cost of training and prediction. ReLU suffices for the purposes of this study, since the focus is on predicting observed behavior.

For the feature space filter, a one-class support vector machine was used to identify extrapolation from the training data prior to making predictions. This can be thought of as detecting outliers in new input features compared to the features used to train the model. Any feature that was missing in more than 60% of the data was dropped from the feature space during training and prediction. Individual data points (i.e., specific timestamps) were dropped if any remaining features were missing values. Derated and offline data were removed from the training dataset but remained in the test dataset. In the partitioning scheme, these features are dropped on a per-model basis.

There are many potential causes for missing data in the SCADA pipeline, and it is difficult to automatically determine what imputation strategy is most appropriate for any particular missing data point. As a result, no imputation is performed during training or prediction. During the prediction stage, all features used in training must be available for a prediction to be made. Any features that were dropped dur-

ing training must be dropped during prediction. Because of the frequency with which missing data occur in the SCADA pipeline, using a large number of features can dramatically reduce the dataset size. By partitioning the farm into small sectors, the waked turbine model is only allowed to depend on a very small number of freestream turbines' signals. This means that the probability that a row has a feature with a missing value is much smaller than if we were to use larger partitions, and this increases the dataset size available for training.

2.6 Validation methodology

In order to close the loop on the model, a validation process was developed to quantify its fitness for use in a controller. Given the need to predict the farm power accurately, one simple validation metric might be some aggregate of the power prediction error. However, it is hard to know what threshold makes for an acceptable model simply by computing this metric over a given dataset.

We therefore took a phenomenological approach to validation, developing metrics and visualizations that test the model's ability to predict important phenomena, namely the ability to predict the following:

- the effects of waking on turbine power (when it occurs and how severely),
- the response of the waked power loss to upstream steering
- the power loss incurred by an upstream steering turbine.

The model must be able to respond to slow transients in the wind conditions and must thus accurately represent when a turbine transitions between waked and non-waked states. Power gains occur over longer timescales, and thus the model should accurately capture the mean power loss due to waking as a function of wind direction, wind speed, and TI. If a model can predict all of these phenomena accurately on a 1 min basis, we assume it will optimize the turbine nacelle positions for wake steering control effectively. Results are presented and discussed in the following sections from this perspective.

3 Results

3.1 Validation results from initial model

We first present some validation results for the initially deployed naive or minimally tuned model to motivate the creation and validation of new variants. As discussed in Sect. 2.6, we seek to model waking and unwaking events dynamically and in aggregate. We inspect our dynamic modeling capabilities through an example time series and then study aggregate modeling through power ratio versus wind direction plots.

One such time series is shown in Fig. 10, which corresponds to a time when wake steering control was enabled. Figure 10a shows the estimated wind direction of a downstream waked turbine (turbine 23, blue) and an upstream wake steering turbine (turbine 11, red). (Refer to Fig. 3 for more details on the turbine numbering and layout.) The horizontal red line in this plot denotes the expected wind direction around which the downstream turbine will be waked by the upstream turbine. In Fig. 10a, we observe a difference in the modeled wind directions of the downstream and upstream turbines, which will complicate our ability to wake steer correctly, since the model needs to account for wake propagation under heterogeneous wind directions. Nevertheless, it is clear that the wind direction is near a direction where the downstream turbine might be waked. Figure 10b shows the yaw error of the upstream turbine. From the high yaw errors of the upstream turbine, we deduce that wake steering occurs throughout much of this time series. (The yaw error of the downstream turbine remains near 0° , indicating that it is not actively wake steering, as expected.) Figure 10c shows SCADA power and model power predictions for these two turbines. We observe that while the model often predicts minimal waking (e.g., at 04:05 UTC, model power predictions of upstream and downstream turbines are similar, suggesting successful wake steering), the actual data tell a different story: the SCADA power value of the downstream turbine is sometimes well below the upstream turbine (e.g., at 04:05 UTC), indicating that strong waking is still present and that our wake steering approach was not successful. Finally, we see that even for the upstream turbine, there are significant differences between the SCADA and model power values. These discrepancies highlight the shortcomings of the initial model and the need for model tuning to perform successful wake steering.

We use power ratio versus wind direction plots (see Sect. 2.4.4) to assess our ability to capture waking and unwaking in aggregate. Reference turbines for this calculation are determined based upon the modified IEC criteria introduced in Sect. 2.4.3. Figure 11 shows the power ratio versus wind direction for turbine 23 (the downstream turbine discussed in the time series plot above), computed over the entire 4 months of our experimental campaign. The data are filtered for wind speeds between 5 and 12 m s^{-1} and powers between 200 and 2500 kW (to ensure region 2 operation). To clarify trends in the data, we use the overlapping binning approach suggested in Fleming et al. (2019), with a bin width of 4° and a step of 2° .

SCADA data and model predictions are shown both when wake steering control is deactivated and when wake steering control is activated. The model and the SCADA show low power ratio values near wind directions of 195° and 210° , indicating that waking is occurring here. However, the strength of waking in the absence of wake steering is significantly over-predicted by the model (much lower power ratios near waking wind directions in the model than in the SCADA

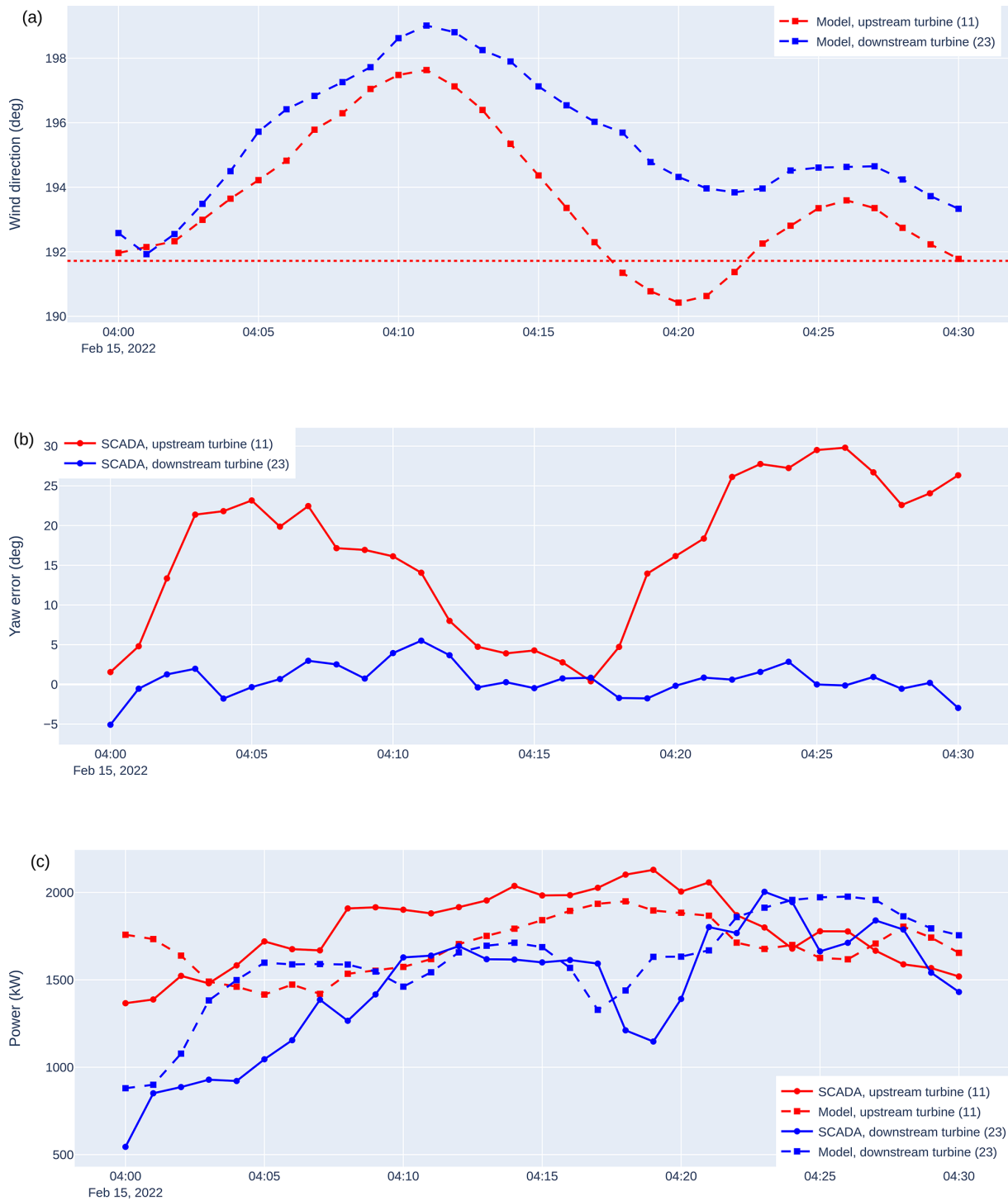


Figure 10. Example time series showing wind direction (a), yaw error (b), and power (c) for an upstream turbine (red) and a downstream turbine (blue). The dashed lines indicate model predictions, and the solid lines indicate SCADA results. The dotted horizontal line in (a) shows a wind direction where the downstream turbine (23) is expected to be waked by the upstream turbine (11).

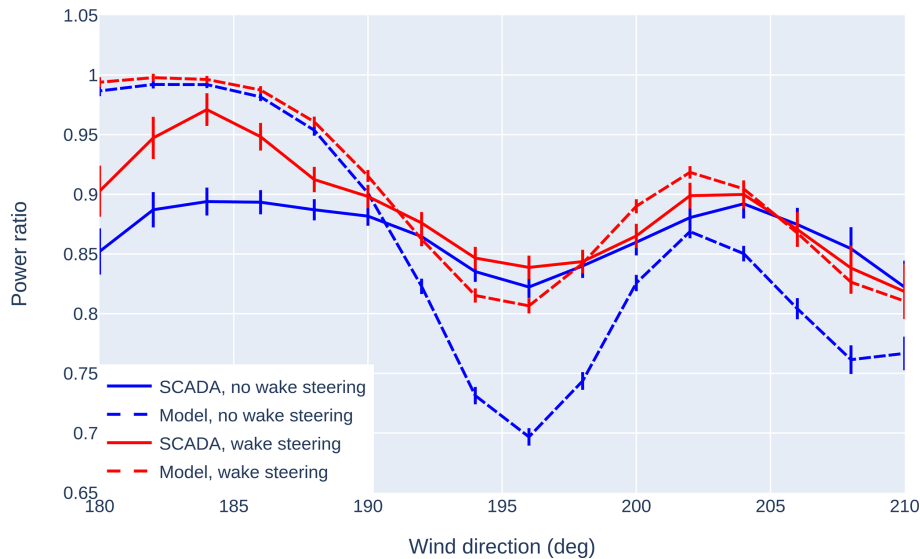


Figure 11. Power ratio versus wind direction for turbine 23 from the SCADA (solid lines) and the model (dashed lines). Results are shown both with wake steering control deactivated (“no wake steering”) and with wake steering control activated (“wake steering”). Error bars correspond to 83 % confidence intervals such that marginally non-overlapping error bars approximate a 95 % statistically significant difference between the means (Goldstein and Healy, 1995).

data). From the SCADA data, we observe an increase in the power ratios when wake steering control is activated, demonstrating that wake steering successfully increases the power of this downstream turbine. However, the differences in power ratios with and without wake steering are much larger in the model than in the SCADA data. This indicates that despite the gains, the model does not properly “understand” the plant behavior and therefore is not able to optimize the plant to its full potential, hence the effort here to improve model predictive capability.

3.2 New models tested

Four additional models were created to be validated against the pilot dataset. These have increasing levels of complexity to demonstrate the value of each component added to the model and the sensitivity to various model parameters.

The selected models are summarized in Table 1. Model 0 is the initial naive model that was deployed during our pilot campaign. Model 1 represents the baseline model for our model tuning study, with no wind direction offsets, farm averaging of the wind speed ($\mathcal{N}_U \rightarrow \infty$), and no output corrector. We then add the estimated wind direction offset in Model 2 to study its effect in isolation. Model 3 is similar to Model 2 but uses a 10 D Gaussian consensus wind speed ($\mathcal{N}_U = 10$) rather than a farm average to study the effect of wind speed heterogeneity. Finally, we use the full output corrector architecture as Model 4. Because neural networks have a high risk of overfitting, Model 4 is a combination of two trained models: one trained on data from 1 December 2021–1 February 2022 and one from 1 February–1 April 2022.

Each model is used to predict the data held out from its training data. We concatenate the two holdout sets to approximate the aggregate performance of Model 4 over the entire time range. It is important to note that this is a conservative test of the output corrector capability, since in a real-world closed-loop application the model would be retrained more frequently; i.e., it would not be used in the controller for months, or even weeks, without being retrained.

3.3 Aggregate metrics

We studied several metrics to compare the overall performance of the models: the mean-squared error of the power signals, mean-squared error of the power ratio signals, correlation coefficient of the power signal, and correlation coefficient of the power ratio signal. All metrics showed similar trends, so for ease of interpretation and comparison, we chose the correlation coefficient of the power ratio (in a 1 min time series sense) as our main metric on which to judge model performance. The correlation coefficient of the power ratio is also strongly affected by modeling errors across the entire plant because incorrect power predictions at the reference turbines will affect the power ratio predicted at all turbines on the farm. The correlation coefficient of the power ratio is computed for each model over different subsets of data and groups of turbines and is shown in Table 2. Quantities were computed over the total validation time range (1 December 2021 to 1 April 2022).

As expected, the initial naive model performance is generally poor, in agreement with our observations in Sect. 3.1. The remaining validations therefore focus on Models 1–4.

Table 1. A description of the parameters used for each model in this study. C_p denotes the source of the power coefficient curve, with OEM indicating that the curves were determined from OEM specifications and SCADA indicating that the curves were determined by fitting to historical SCADA data. Wind direction source gives the wind direction source. $\Delta\theta$ is the estimated wind direction offset. N_U and N_θ denote the wind speed and wind direction spatial filter widths, respectively. The TI mapping column indicates whether a TI mapping is used. (The details of the TI mapping for Model 0 are given in Sect. 2.4.5.) The output corrector column indicates whether the output corrector is used.

ID	C_p	Wind direction source	$\Delta\theta$	N_U	N_θ	TI mapping	Output corrector
0	OEM	SCADA and GNSS compass	0°	∞	5	Yes	No
1	SCADA	GNSS compass	0°	∞	∞	No	No
2	SCADA	GNSS compass	5°	∞	∞	No	No
3	SCADA	GNSS compass	5°	10	∞	No	No
4	SCADA	GNSS compass	5°	10	∞	No	Yes

Table 2. The correlation coefficient of the power ratio for different models. Because different models will differ in terms of the impact on freestream power estimation and waked power estimation, we decompose the dataset into different wind direction sectors and waking/waked turbine clusters. “Full wind sector, all turbines” shows overall performance. “Wind from the south, all turbines” focuses on all turbines for the waking wind sector of interest (wind directions from 152 to 242° and wind speeds from 5 to 12 m s⁻¹). “Wind from the south, turbines 8–13” considers the performance of predicting upstream turbines that may wake the second-row turbines. “Wind from the south, turbines 19–24” examines the performance of predicting turbines that may be waked in the second row.

Model number	0	1	2	3	4
Data subset					
Full wind sector, all turbines	0.058	0.058	0.063	0.173	0.837
Wind from the south, all turbines	0.048	0.068	0.083	0.779	0.894
Wind from the south, turbines 8–13	0.058	0.089	0.087	0.748	0.933
Wind from the south, turbines 19–24	0.158	0.096	0.199	0.474	0.724

Starting from the baseline model (Model 1), the aggregate metrics generally improve with each addition to the modeling framework, and this improvement holds across most subsets of the data. The addition of the wind direction offset (Model 1 to Model 2) improves the power ratio correlation coefficients slightly for all turbines in the full wind sector. By examining the subsets of the data, we see that this change is driven by improvements to second-row turbines (19–24) and that front-row turbines (8–13) show negligible differences (the slight differences observed are likely just due to differences in the reference turbines, which change as the wind direction changes), as expected.

Allowing wind speed heterogeneity (Model 2 to Model 3) substantially improves the correlation coefficients for two reasons. The first is an improvement in modeling the reference turbine powers in the front row, which is evident from the large increase in correlation coefficients across upstream turbines 8–13, from 0.087 to 0.748. The second is an improvement in modeling the local ambient wind speeds that the engineering wake model uses to derive the wake deficit, which can be seen from the moderate increase in correlation coefficients across downstream turbines 19–24, from 0.199 to 0.474. Since Model 3 shows larger correlation coefficients on upstream turbines (0.748) than on downstream turbines (0.474), we conclude that this model is more success-

ful in predicting upstream turbine power than downstream turbine power.

The output corrector model (Model 4) shows the best performance across all data subsets. The correlation coefficient for Model 4 is about 0.7 to 0.9 (depending on the dataset considered), indicating excellent agreement between this model and the observations, demonstrating the value of this hybrid approach in improving a model’s understanding over time. Additionally, the greatly improved performance of Model 3 over Models 1 and 2 highlights the potential for deploying an initial model without an output corrector, providing reasonable accuracy while enough wake steering observations are collected to train the output corrector to the point where it can make predictions on the effects of various yaw misalignments.

3.4 Power ratio versus wind direction

Figure 12 shows the power ratio as a function of the SCADA wind direction when wake steering was disabled for two representative waked turbines: 19 and 24. The data have been filtered for region 2 wind conditions and for times when wake steering control was toggled off, yielding about 2 to 3 weeks of data over the 4-month measurement period. As in Fig. 11, we use overlapping bins (4° bin width and 2° bin step) to reduce noise in the data.

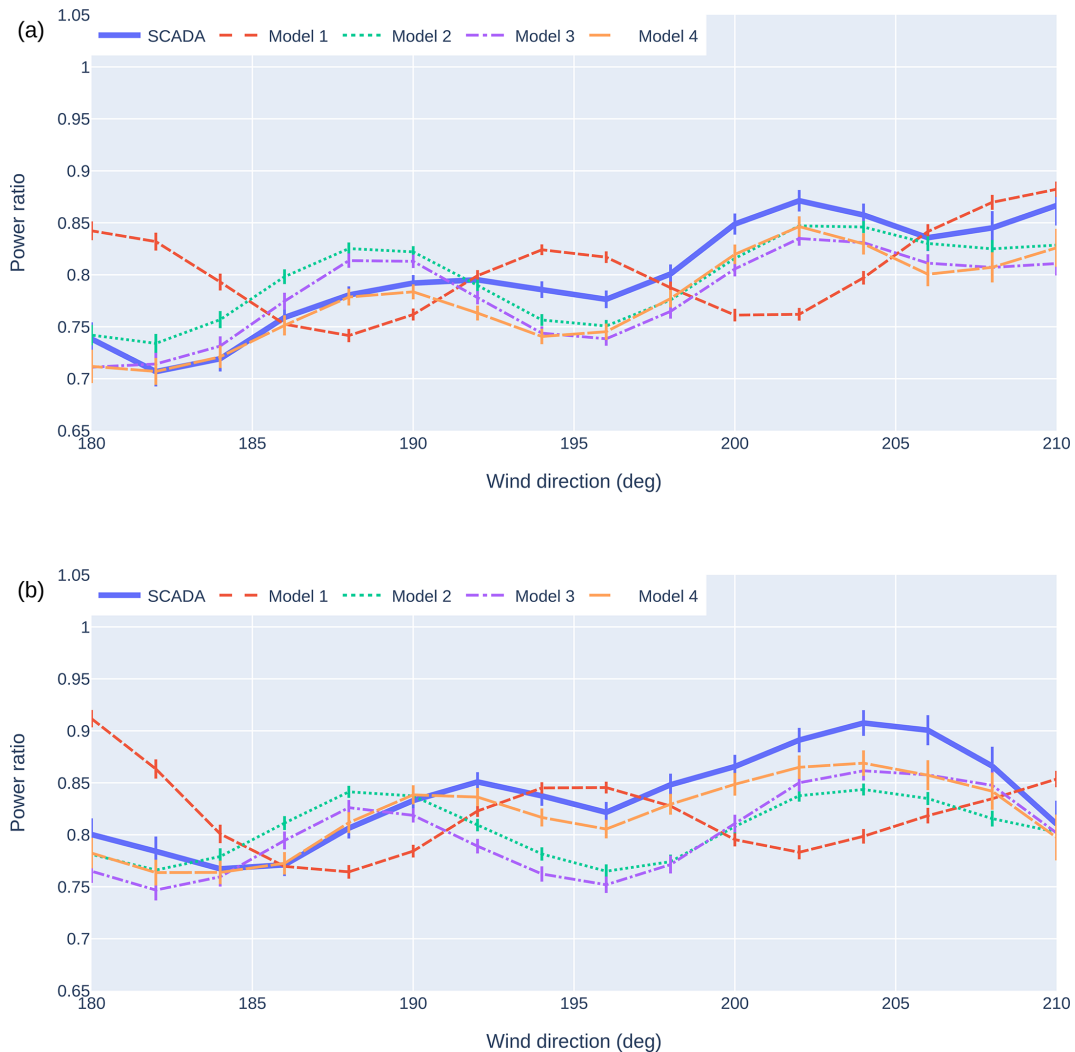


Figure 12. The power ratio as a function of a turbine’s SCADA wind direction from SCADA and various models for turbines 19 (a) and 24 (b) when wake steering is disabled. Error bars correspond to 83 % confidence intervals such that marginally non-overlapping error bars approximate a 95 % statistically significant difference between the means (Goldstein and Healy, 1995). Models 2 and 3, which differ in wind speed heterogeneity, show similar patterns of waking behavior but different magnitudes. The output corrector model (Model 4) differs from other models in magnitude for both turbines and in phase for turbine 24. The baseline model (Model 1) shows a relatively large phase shift with respect to the SCADA data.

Wind directions with low power ratios in Model 1 are offset from those in the SCADA, indicating that this model does not capture wake locations properly. (For example, Model 1 shows a trough in the power ratio at 188° in Fig. 12a, whereas the SCADA shows a peak in the power ratio here.) By including the wind direction offset, Model 2 significantly improves predictions of wake locations, especially for turbine 19 in Fig. 12a. However, we still observe misalignment in some peak and trough locations between Model 2 and the SCADA for turbine 24 in Fig. 12b. (For example, Model 2 shows a peak at 188° , while the SCADA shows a peak at 192° .)

Model 3 (which introduces wind speed heterogeneity) shows similar peak and trough locations to Model 2 but with

different power ratio magnitude values. This suggests that wind speed heterogeneity does not have a significant impact on downstream waking locations but may affect the expected power losses. While the overall metrics in Sect. 3.3 indicate that Model 3 performs better on downstream turbines, the power ratio results do not show a clear improvement in accuracy with Model 3. Model 4 shows the closest match in peak and trough locations in the SCADA, particularly in Fig. 12b, indicating that the output corrector model gives the best prediction of waking and unwaking trends.

In Fig. 13, we consider these same plots for times when wake steering was enabled. This will allow us to assess if our model tuning process also improves the accuracy when up-

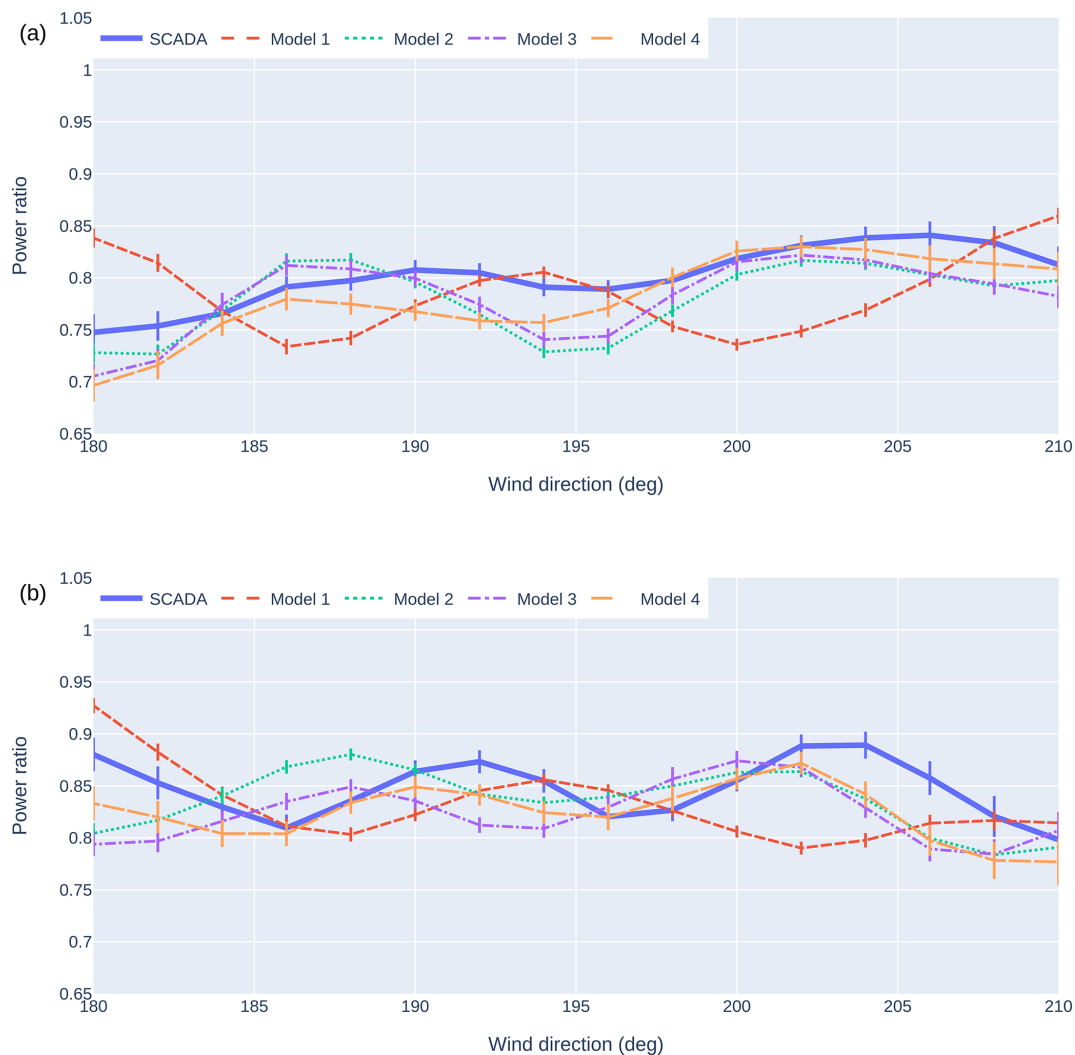


Figure 13. The power ratio as a function of a turbine’s SCADA wind direction from SCADA and various models for turbine 19 (a) and 24 (b) when wake steering is enabled. Error bars correspond to 83 % confidence intervals such that marginally non-overlapping error bars approximate a 95 % statistically significant difference between the means (Goldstein and Healy, 1995).

stream turbines may yaw to steer downstream wakes. The results mirror those with wake steering disabled. As before, we observe that the wind direction offset generally improves our modeling of wake locations (e.g., compare the power ratio predictions at 200° among SCADA, Model 1, and Model 2 in Fig. 13a), but there is some slight misalignment for turbine 24 near 190° in Fig. 13b. Also as before, while the power ratio values differ between Models 2 and 3, the peak and trough locations are similar, and Model 3 does not represent a clear improvement from Model 2. The peak and trough locations from Model 4 most closely match the SCADA for both turbine 19 and turbine 24, indicating that the output corrector model is expected to give the best predictions of wake locations, but discrepancies still exist when comparing Model 4 to SCADA values.

Finally, Fig. 14 shows binned mean power ratio predictions versus wind direction for turbine 23, for comparison with the initial deployed model predictions shown in Fig. 11. We see again how Model 1 fails to predict the correct wake locations. Models 2 and 3 appear to overestimate the impact of waking and the benefit from wake steering, while Model 4 shows the closest agreement with the observed performance.

3.5 Time series

We finally consider two time series in detail in an anecdotal examination of model performance. For the first time series, we consider a case without wake steering, and for the second time series, we consider a case with wake steering.

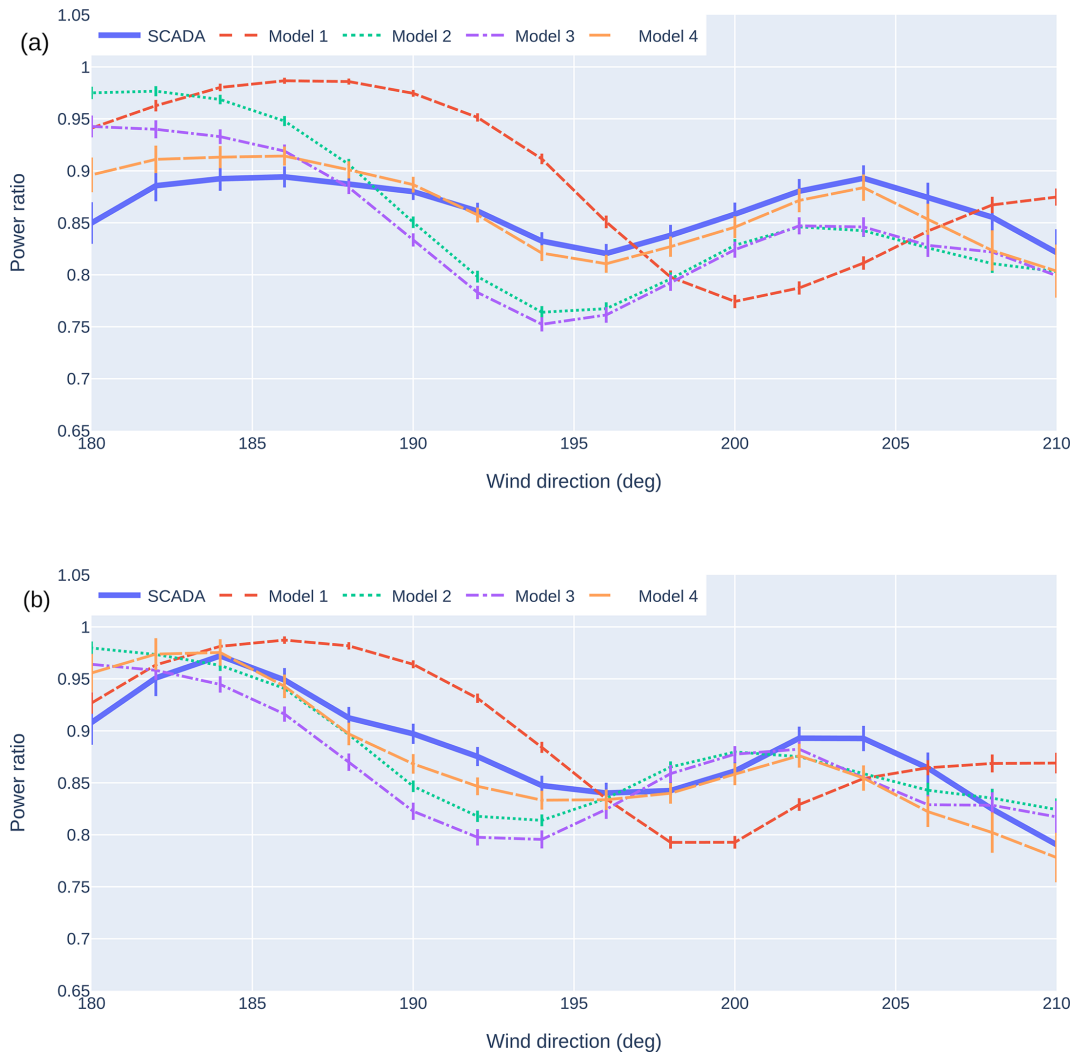


Figure 14. Turbine 23’s power ratio as a function of its own SCADA wind direction computed with various models with wake steering disabled **(a)** and enabled **(b)**, for comparison to the initial deployed model performance shown in Fig. 11.

3.5.1 Time series without wake steering

Figures 15 and 16 compare SCADA results and model predictions for a representative time series when wake steering control was disabled. Figure 15 shows results for turbine 10 (an upstream turbine). As expected, adding the wind direction offset (Model 1 to Model 2) has a negligible effect, since this turbine is unwaked. While the power predictions from Models 1–3 follow the same trend, Model 3 matches the SCADA power values most closely, indicating that introducing wind speed heterogeneity into the model improves the predictions at upstream turbines, in agreement with our findings in Sect. 3.3. Model 4 has the strongest correlation with the underlying SCADA time series and gives the most accurate power predictions, as expected, since it involves machine learning on real-world operational data. However, Model 4 predictions lag the measured power by about 1 min and exhibit slightly higher power values throughout much of

the time series. While the reason for the time lag is unclear, the biased power values indicate that this turbine produced higher power in the training period in comparable wind conditions. This bias is not expected to be an issue in a field deployment of this model architecture, since the deployed model would continually be retrained based on the latest available data and would thus be less affected by historical changes in turbine performance.

Model 4’s discrepancies highlight the challenges of interpreting machine learning models, which would ideally have errors that are not correlated in time. In other words, a correctly specified model will have errors that appear to be independent and identically distributed, as well as zero mean Gaussian noise. When model errors (residuals) are correlated with one of the input features (in this case, time), then there is typically an opportunity to improve the model.

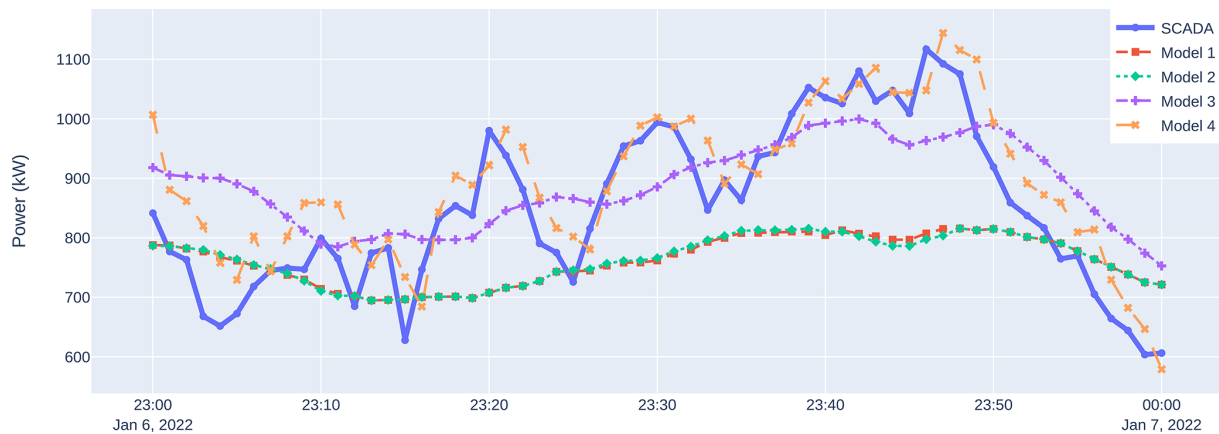


Figure 15. Example time series showing the power of turbine 10 when wake steering is disabled. Turbine 10 is a freestream turbine in this sector. SCADA results are compared against the predictions from various models from Table 1.

While we can hypothesize about how the model makes predictions, it is more difficult to understand why the model converged to a particular solution. A strong case can be made that the time-lagged target turbine's power is a strong predictor of the most recent power, and the model just makes small perturbations to the time-lagged power signal (which is the intent of the feature space design). A case can also be made that the advection time causes the observed time lag. However, the goal is to determine how to improve the model, but it is unclear why the model fails to converge to a non-time-lagged solution in our current implementation, since it should have the necessary features to do so. Potential paths forward could be additional feature engineering, such as including additional time lags, collecting more training data, and/or adjusting the model hyperparameters.

Figure 16 shows results for turbine 22 (the turbine downstream of turbine 10). From Fig. 16(a), we see that this turbine will encounter one wakening wind direction (dashed horizontal line) over this hour. Model 1 (which has no wind direction offset) predicts that we cross this wind direction at 23:45 UTC and then transition to a wind direction with less wakening (23:50 UTC to the end). Models 2 and 3 (which include the $+5^\circ$ wind direction offset) predict that we will reach this wind direction and remain there for the final 10 min of the time series.

The power ratio and power predictions (Fig. 16b and c, respectively) provide a good test of these models. Model 1 predicts that wakening occurs from about 23:30 to 23:45 UTC (power ratios below 1) and is not present near the end of the time series. The SCADA data, however, show that wakening occurs from about 23:45 UTC to the end of the time series, highlighting the potential for detrimental control decisions if Model 1 were to be used in a wake steering controller. Model 2 captures this trend very well, suggesting that the wind direction offset has enabled us to successfully predict the dynamic onset of wakening. Model 3 shows very similar results to Model 2 and thus that including wind speed hetero-

geneity has little effect on this downstream turbine (in contrast to the benefit it provided on the corresponding upstream turbine).

While Models 2 and 3 substantially improve wakening predictions near the end of this time series, discrepancies remain between these models and the SCADA early in the time series. For example, at 23:15 UTC, the SCADA shows low power ratios and powers for this turbine, which do not seem to be explained by wakening. Model 4, however, is generally able to capture these trends well, indicating that our output corrector approach can represent phenomena beyond what can be captured in an EWM (e.g., large levels of flow heterogeneity or rapid-flow transients). As before, Model 4 has an apparent 1 min time lag and some biased power values, the latter of which may be due to changes in turbine performance from the training period. Again, this is a conservative test of the output corrector since it was not trained on the 2-month period that contains this time series.

3.5.2 Time series with wake steering

Figures 17 and 18 compare SCADA results and model predictions for a representative time series when wake steering was activated (the same time series considered in Fig. 10). Figure 17 shows results for turbine 11 (an upstream turbine that is wake steering). As can be observed in Sect. 3.5.1, adding the wind direction offset (Model 1 to Model 2) has a negligible effect here, and introducing wind speed heterogeneity (Model 2 to Model 3) improves the power predictions. Model 4 again correlates well with the underlying SCADA signal; however, there is a slight bias toward the power predictions that we attribute to different turbine performance in the training period, which could be addressed by retraining the model on the latest data.

Figure 18 shows results for turbine 23 (the turbine downstream of turbine 11). From Fig. 18a, we see that Model 1 expects turbine 23 to be significantly wakened by turbine 11 and



Figure 16. Example time series showing wind direction (a), power ratio (b), and power (c) for turbine 22 for a time when wake steering is disabled. SCADA results are compared against the predictions from various models from Table 1. The dotted horizontal line in (a) shows a wind direction where the downstream turbine (22) is expected to be waked by the upstream turbine (10). Several drops in power ratio occur throughout the time series, likely due to a combination of heterogeneity and waking on short timescales.

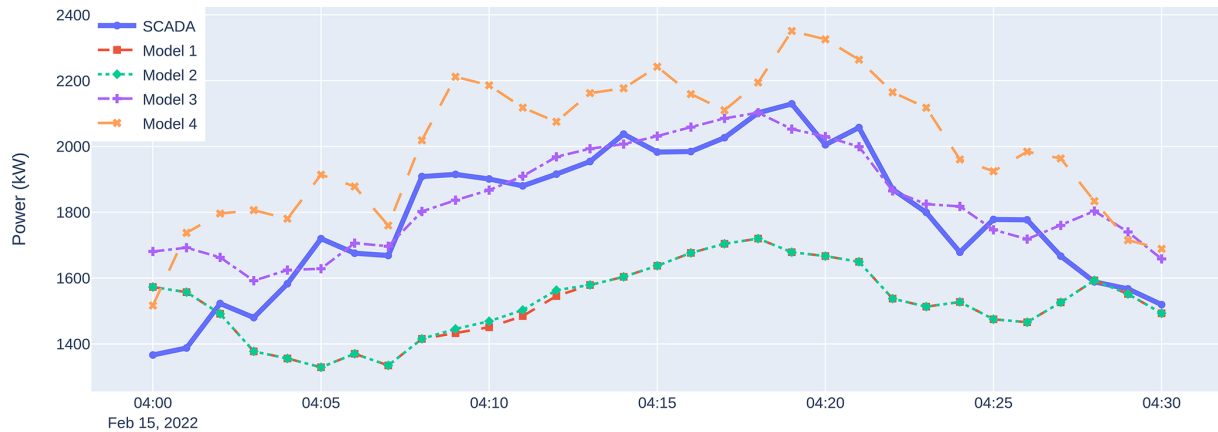


Figure 17. Example time series showing the power of turbine 11 when it is steering. SCADA results are compared against the predictions from various models from Table 1.

thus predicts a power ratio below 1 for the entire time range considered (Fig. 18b). The SCADA data, however, show that the power ratio fluctuates between a value near 1 (indicating no waking) and a value below 1 (indicating waking). Models 2 and 3 include the $+5^\circ$ wind direction offset, shifting the model wind direction (Fig. 18a) above that at which we expect significant waking. As a result, the model power ratios are larger and closer to the SCADA data over much of the time range. One exception is at the start of the time series (04:00 UTC), where the SCADA shows much lower power values than the models. The cause of this discrepancy is unclear, since the average wind directions and TIs (not shown) are similar to those at later times when there are higher powers (04:20 UTC). As before, we expect this phenomenon to be driven by wind condition transients or heterogeneity levels that are not captured by our engineering wake model. Finally, we see that while allowing wind speed heterogeneity (Model 2 to Model 3) changes the power and power ratio predictions of the downstream turbine, it does not substantially improve the model accuracy at the downstream turbine for this particular time series. Model 4 shows strong correlation with the observations and successfully captures additional information missed by Models 1–3. Though the dataset does not contain enough operations similar to this scenario to evaluate the downstream turbine’s energy gain in aggregate, this should be a focus of future work, along with the ability to predict the upstream turbine’s power loss, in order to assess the model’s effectiveness at predicting the total impact of wake steering.

3.6 Suitability for optimization

Despite doing better at predicting the 1 min behavior of the plant power, the models must also be assessed for their suitability to be used with an optimization algorithm to find the optimum yaw values for all steerable turbines. Given that all models except Model 4 use an analytical formulation de-

signed to be continuous for gradient-based optimization, it can be assumed that they will not cause any problems therein. However, Model 4 had to be tested to ensure its predictions of farm power remained smooth in the yaw angle dimension.

Figure 19 shows the resulting farm power gain predicted over a parameter sweep of turbine 13’s yaw angle. We refer to the predicted farm power gain due to yawing a single turbine. The numerator is the sum of each turbine’s power caused by changing only turbine 13’s yaw angle. The denominator is the sum of each turbine’s power with all yaw angles set at zero. Behind the scenes, there is a suite of machine learning models being used to recompute the power at each individual turbine (one model per turbine). Only a small subset of downstream turbines’ powers (hopefully one or two, depending on the wake width) depends on this freestream turbine’s yaw error. Only one upstream turbine’s power depends on this yaw angle (the turbine whose yaw angle is being adjusted). When this individual model reverts back to the engineering wake model, the predicted power for the affected subset changes significantly. The other turbines’ powers remain at their adjusted values. Therefore, between Models 3 and 4, the numerator and the denominator are very different values, even when a single machine learning reverts back to using only the EWM. The difference in bias between the underlying EWM and the machine learning model is the cause of the discontinuity.

A wake steering controller would roughly want to find the maximum of this function in order to prescribe optimum yaw values. We see that there is a discontinuity in the results with the output corrector, highlighting the effectiveness of the feature space filter in preventing extrapolation beyond the training data. However, we also see the potential for “trapping” the controller output if the discontinuity were reversed such that it might never prescribe larger yaw angles, and therefore the output corrector would not be able to learn from observations at these larger yaw angles. This is not the case in Fig. 19; i.e., the feature-space-filtered EWM results would

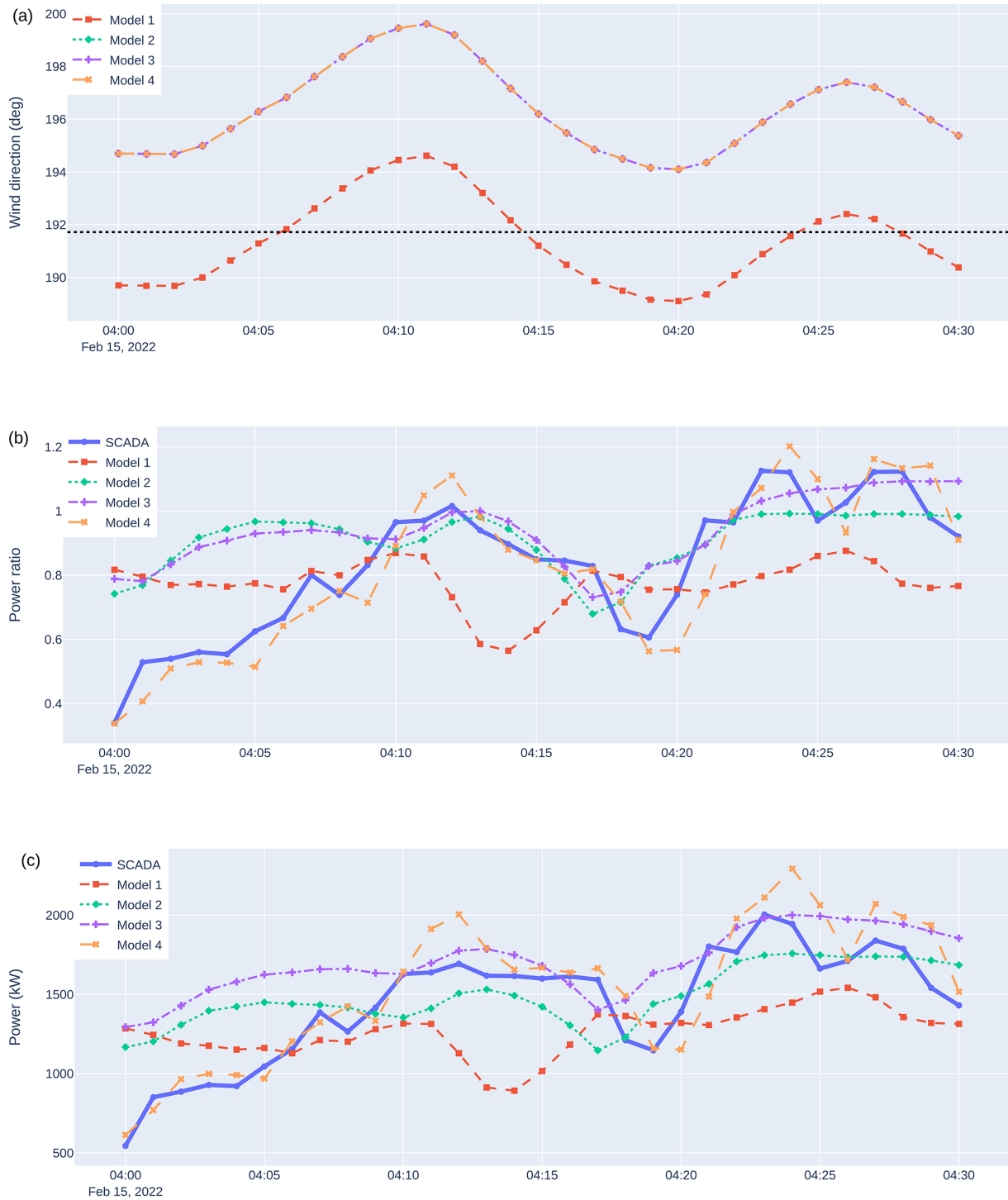


Figure 18. Example time series showing wind direction (a), power ratio (b), and power (c) for turbine 23, which is downstream of a turbine that is wake steering (turbine 11). SCADA results are compared against the predictions from various models from Table 1. The dotted horizontal line in (a) shows a wind direction where the downstream turbine (23) is expected to be waked by the upstream turbine (11).

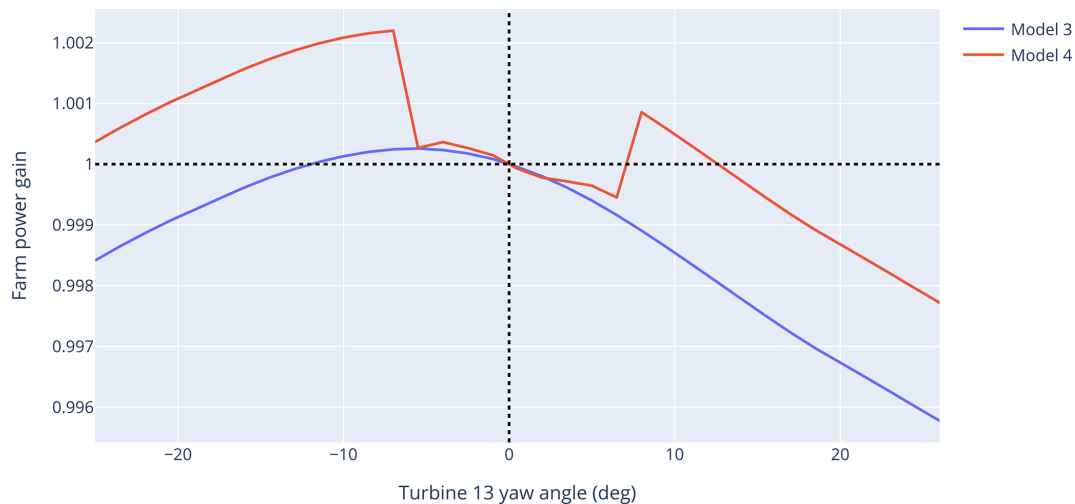


Figure 19. Predictions of farm power gain as a function of turbine 13's yaw angle with and without the output corrector (Models 4 and 3, respectively). For Model 4, the full output corrector is used for yaw error values between -6 and $+7^\circ$. Outside of this range, all individual models in the ensemble will revert back to the engineering wake model, if that model depends on turbine 13's yaw error. All other models in the output corrector ensemble are used for the entire range.

inspire a larger yaw angle, but this may not always be the case. To this end, further work may be required to ensure predictions are smooth in the yaw angle dimension or to detect times when yaw angles are being limited by the discontinuity such that the EWM can be used to further explore the feature space.

One final consideration is computational cost. The changes made to get to Model 3 from Models 1 and 2 do not appreciably increase computational cost, allowing for a real-time optimization to be computed in less than 1 min. The output corrector, however, adds costs from the model selection logic, neural network prediction, and feature space filtering. In the form tested here, this increases the time to run a wake steering optimization several-fold. This is certainly not insurmountable given the potential of neural networks to use higher-performance libraries and GPU hardware and/or to store information about the gradient of the target with respect to features (namely yaw in our case), which negates the need to use a finite difference to compute gradients as in the implementation tested here.

4 Conclusions

A model-based wake steering control system was developed and deployed to 10 turbines on a 58-turbine wind farm with 13 rotor diameter spacing in the predominant wind direction – to the best of our knowledge the largest and most complex wake steering campaign to date. Wake steering was achieved through absolute nacelle position control, eliminating the shortcomings of control via yaw offsets applied to a turbine's own measurement of the wind direction. Initial results from the pilot study showed power gains at the selected

downstream turbines as a result of wake steering, though as expected, the preliminary minimally tuned model was not able to perfectly predict and therefore optimize the plant behavior. Based on the collected wake steering dataset, we developed a novel model architecture and validation approach to close the loop in order to improve the predictive capability and therefore wake steering performance over time. The validation approach included high-level aggregate metrics (on the entire farm and on important subsets of the data), a power ratio binned by wind direction for waked turbines, and a detailed examination of key time series in the operational data.

It was shown that the most simplistic model provided poor predictions of plant behavior, indicating the importance of this validation process for effective control. As complexity was added to the model, predictive capability improved. The most accurate model included a data-driven wind direction offset calibration, a Gaussian spatial filter to allow for wind speed heterogeneity, and a neural-network-based output corrector. However, even without the output corrector, it was shown that it is possible to achieve substantial improvements with data-driven engineering wake model input estimation/calibration.

The output corrector results show great promise for leveraging the rapidly advancing fields of artificial intelligence and machine learning in order to develop more effective wind farm control systems. In this study a relatively simple neural network architecture was employed, and some weaknesses of the approach were highlighted, namely the additional computational cost required to make predictions and the potential for discontinuous outputs between the neural networks and the engineering wake model in the space of the optimization actuation variable (yaw angle). However, there is a vast

array of new avenues to explore in future work: introducing more complex neural network models designed for forecasting (such as long short-term memory or transformers) to enable a “preview” of wind direction like that simulated in Sengers et al. (2023), imposing physical constraints on the models, or using learned gradient information for efficient optimization.

Future work should also focus on testing the model’s ability to predict the change in the downstream turbine power and power ratio due to wake steering – not only its absolute value – both in a time series sense and in aggregate. Once enough operational data have been accumulated, the overall energy gain of the entire control system should also be evaluated, taking into account upstream turbine losses due to yaw.

Data availability. Because this work was carried out as part of the development of a commercial product, data are not openly available, as this would reduce the competitive advantage of WindESCo in the market.

Author contributions. PB, PI, and BB wrote the software to create and validate the wake models, along with the centralized wind farm control software that makes use of these wake models. PB, PI, and BB also wrote the code to process and visualize the data collected. CQ developed the feature space filtering and Gaussian consensus algorithms and code and helped with machine learning model selection and training. DZ managed the installation and debugging of the hardware and software at the site, as well as the development of the turbine-level software interfaces. MD secured the resources for and helped plan the project. All authors contributed to the writing and editing of the paper.

Competing interests. The authors are affiliated with WindESCo, Inc.

Disclaimer. Publisher’s note: Copernicus Publications remains neutral with regard to jurisdictional claims made in the text, published maps, institutional affiliations, or any other geographical representation in this paper. While Copernicus Publications makes every effort to include appropriate place names, the final responsibility lies with the authors.

Acknowledgements. The authors would like to acknowledge Longroad Energy for their support in carrying out this project. The authors would also like to acknowledge Brendan Taylor and Nathan Post for their efforts in developing and installing the pilot system.

Review statement. This paper was edited by Katherine Dykes and reviewed by two anonymous referees.

References

- Ahmad, T., Basit, A., Ahsan, M., Coupiac, O., Girard, N., Kazemtabrizi, B., and Matthews, P. C.: Implementation and analyses of yaw based coordinated control of wind farms, *Energies*, 12, 1266, <https://doi.org/10.3390/en12071266>, 2019.
- Andersson, L. E., Anaya-Lara, O., Tande, J. O., Merz, K. O., and Imsland, L.: Wind farm control – Part I: A review on control system concepts and structures, *IET Renew. Power Generat.*, 15, 2085–2108, 2021.
- Bastankhah, M. and Porté-Agel, F.: Experimental and theoretical study of wind turbine wakes in yawed conditions, *J. Fluid Mech.*, 806, 506–541, 2016.
- Bensason, D., Simley, E., Roberts, O., Fleming, P., Debnath, M., King, J., Bay, C., and Mudafort, R.: Evaluation of the potential for wake steering for U.S. land-based wind power plants, *Journal of Renewable and Sustainable Energy*, 13, 033303, <https://doi.org/10.1063/5.0039325>, 2021.
- Campagnolo, F., Weber, R., Schreiber, J., and Bottasso, C. L.: Wind tunnel testing of wake steering with dynamic wind direction changes, *Wind Energ. Sci.*, 5, 1273–1295, <https://doi.org/10.5194/wes-5-1273-2020>, 2020.
- Campagnolo, F., Imširović, L., Braunbehrens, R., and Bottasso, C. L.: Further calibration and validation of FLORIS with wind tunnel data, in: *J. Phys. Conf. Ser.*, 2265, 022019, <https://doi.org/10.1088/1742-6596/2265/2/022019>, 2022.
- Crespo, A. and Hernandez, J.: Turbulence characteristics in wind-turbine wakes, *J. Wind Eng. Indust. Aerodynam.*, 61, 71–85, 1996.
- Debusscher, C. M. J., Göçmen, T., and Andersen, S. J.: Probabilistic surrogates for flow control using combined control strategies, *J. Phys. Conf. Ser.*, 2265, 032110, <https://doi.org/10.1088/1742-6596/2265/3/032110>, 2022.
- Doekemeijer, B. M., van der Hoek, D., and van Wingerden, J.-W.: Closed-loop model-based wind farm control using FLORIS under time-varying inflow conditions, *Renew. Energy*, 156, 719–730, 2020.
- Doekemeijer, B. M., Kern, S., Maturu, S., Kanev, S., Salbert, B., Schreiber, J., Campagnolo, F., Bottasso, C. L., Schuler, S., Wilts, F., Neumann, T., Potenza, G., Calabretta, F., Fioretti, F., and van Wingerden, J.-W.: Field experiment for open-loop yaw-based wake steering at a commercial onshore wind farm in Italy, *Wind Energ. Sci.*, 6, 159–176, <https://doi.org/10.5194/wes-6-159-2021>, 2021.
- Doekemeijer, B. M., Simley, E., and Fleming, P.: Comparison of the Gaussian wind farm model with historical data of three offshore wind farms, *Energies*, 15, 1964, <https://doi.org/10.3390/en15061964>, 2022.
- Dong, H., Xie, J., and Zhao, X.: Wind farm control technologies: from classical control to reinforcement learning, *Prog. Energy*, 4, 032006, <https://doi.org/10.1088/2516-1083/ac6cc1>, 2022.
- EIA: Tracking Clean Energy Progress 2023, Tech. rep., EIA, <https://www.iea.org/reports/tracking-clean-energy-progress-2023> (last access: 19 December 2023), 2023.
- Fleming, P., Annoni, J., Shah, J. J., Wang, L., Ananthan, S., Zhang, Z., Hutchings, K., Wang, P., Chen, W., and Chen, L.: Field test of wake steering at an offshore wind farm, *Wind Energ. Sci.*, 2, 229–239, <https://doi.org/10.5194/wes-2-229-2017>, 2017.

- Fleming, P., King, J., Dykes, K., Simley, E., Roadman, J., Scholbrock, A., Murphy, P., Lundquist, J. K., Moriarty, P., Fleming, K., van Dam, J., Bay, C., Mudafort, R., Lopez, H., Skopek, J., Scott, M., Ryan, B., Guernsey, C., and Brake, D.: Initial results from a field campaign of wake steering applied at a commercial wind farm – Part 1, *Wind Energ. Sci.*, 4, 273–285, <https://doi.org/10.5194/wes-4-273-2019>, 2019.
- Fleming, P., King, J., Simley, E., Roadman, J., Scholbrock, A., Murphy, P., Lundquist, J. K., Moriarty, P., Fleming, K., van Dam, J., Bay, C., Mudafort, R., Jager, D., Skopek, J., Scott, M., Ryan, B., Guernsey, C., and Brake, D.: Continued results from a field campaign of wake steering applied at a commercial wind farm – Part 2, *Wind Energ. Sci.*, 5, 945–958, <https://doi.org/10.5194/wes-5-945-2020>, 2020.
- Gebraad, P. M., Teeuwisse, F. W., Van Wingerden, J., Fleming, P. A., Ruben, S. D., Marden, J. R., and Pao, L. Y.: Wind plant power optimization through yaw control using a parametric model for wake effects – a CFD simulation study, *Wind Energy*, 19, 95–114, 2016.
- Goldstein, H. and Healy, M. J. R.: The Graphical Presentation of a Collection of Means, *J. Roy. Stat. Soc. A*, 158, 175–177, 1995.
- Howland, M. F.: Wind farm yaw control set-point optimization under model parameter uncertainty, *J. Renew. Sustain. Energ.*, 13, 043303, <https://doi.org/10.1063/5.0051071>, 2021.
- Howland, M. F., Lele, S. K., and Dabiri, J. O.: Wind farm power optimization through wake steering, *P. Natl. Acad. Sci. USA*, 116, 14495–14500, 2019.
- Howland, M. F., Ghate, A. S., Lele, S. K., and Dabiri, J. O.: Optimal closed-loop wake steering – Part 1: Conventionally neutral atmospheric boundary layer conditions, *Wind Energ. Sci.*, 5, 1315–1338, <https://doi.org/10.5194/wes-5-1315-2020>, 2020.
- Howland, M. F., Ghate, A. S., Quesada, J. B., Pena Martínez, J. J., Zhong, W., Larrañaga, F. P., Lele, S. K., and Dabiri, J. O.: Optimal closed-loop wake steering – Part 2: Diurnal cycle atmospheric boundary layer conditions, *Wind Energ. Sci.*, 7, 345–365, <https://doi.org/10.5194/wes-7-345-2022>, 2022a.
- Howland, M. F., Quesada, J. B., Martínez, J. J. P., Larrañaga, F. P., Yadav, N., Chawla, J. S., Sivaram, V., and Dabiri, J. O.: Collective wind farm operation based on a predictive model increases utility-scale energy production, *Nat. Energ.*, 7, 818–827, 2022b.
- IEC: IEC 61400-12-1(2): Wind energy generation systems – Part 12-1: Power performance measurements of electricity producing wind turbines, Standard, International Electrotechnical Commission, Geneva, Switzerland, 2017.
- Kanev, S. K.: AWC validation methodology, Report, TNO, <http://resolver.tudelft.nl/uuid:fdae4c94-fbcc-4337-b49f-5a39c93ef2cf> (last access: 19 December 2023), 2020.
- King, J., Fleming, P., King, R., Martínez-Tossas, L. A., Bay, C. J., Mudafort, R., and Simley, E.: Control-oriented model for secondary effects of wake steering, *Wind Energ. Sci.*, 6, 701–714, <https://doi.org/10.5194/wes-6-701-2021>, 2021.
- Kumar, D., Rotea, M. A., Aju, E. J., and Jin, Y.: Wind plant power maximization via extremum seeking yaw control: A wind tunnel experiment, *Wind Energy*, 26, 283–309, <https://doi.org/10.1002/we.2799>, 2023.
- Lee, J. C. Y. and Fields, M. J.: An overview of wind-energy-production prediction bias, losses, and uncertainties, *Wind Energ. Sci.*, 6, 311–365, <https://doi.org/10.5194/wes-6-311-2021>, 2021.
- Liew, J., Urbán, A. M., and Andersen, S. J.: Analytical model for the power–yaw sensitivity of wind turbines operating in full wake, *Wind Energ. Sci.*, 5, 427–437, <https://doi.org/10.5194/wes-5-427-2020>, 2020.
- Meyers, J., Bottasso, C., Dykes, K., Fleming, P., Gebraad, P., Giebel, G., Göçmen, T., and van Wingerden, J.-W.: Wind farm flow control: prospects and challenges, *Wind Energ. Sci.*, 7, 2271–2306, <https://doi.org/10.5194/wes-7-2271-2022>, 2022.
- Niayifar, A. and Porté-Agel, F.: Analytical Modeling of Wind Farms: A New Approach for Power Prediction, *Energies*, 9, 741, <https://doi.org/10.3390/en9090741>, 2016.
- NREL: FLORIS (version 2.4), GitHub [code], <https://github.com/NREL/floris> (last access: 19 December 2023), 2021.
- Pedregosa, F., Varoquaux, G., Gramfort, A., Michel, V., Thirion, B., Grisel, O., Blondel, M., Prettenhofer, P., Weiss, R., Dubourg, V., Vanderplas, J., Passos, A., Cournapeau, D., Brucher, M., Perrot, M., and Duchesnay, E.: Scikit-learn: Machine Learning in Python, *J. Mach. Learn. Res.*, 12, 2825–2830, 2011.
- Post, N., Taylor, B. F., Bachant, P., Kossuth, J. A., and Dua, M.: Methods and systems of advanced yaw control of a wind turbine, US Patent, 0 243 699, 2022.
- Post, N. L., Zheng, D., Bachant, P., and Dua, M.: Systems and methods of coordinate yaw control of multiple wind turbines, US Patent, 0 272 775, 2023.
- Rosencrans, D., Lundquist, J. K., Optis, M., Rybchuk, A., Bordini, N., and Rossol, M.: Seasonal variability of wake impacts on US mid-Atlantic offshore wind plant power production, *Wind Energ. Sci.*, 9, 555–583, <https://doi.org/10.5194/wes-9-555-2024>, 2024.
- Sengers, B. A. M., Rott, A., Simley, E., Sinner, M., Steinfeld, G., and Kühn, M.: Increased power gains from wake steering control using preview wind direction information, *Wind Energ. Sci.*, 8, 1693–1710, <https://doi.org/10.5194/wes-8-1693-2023>, 2023.
- Simley, E., Fleming, P., Girard, N., Alloin, L., Godefroy, E., and Duc, T.: Results from a wake-steering experiment at a commercial wind plant: investigating the wind speed dependence of wake-steering performance, *Wind Energ. Sci.*, 6, 1427–1453, <https://doi.org/10.5194/wes-6-1427-2021>, 2021.
- Smith, B., Link, H., Randall, G., and McCoy, T.: Applicability of nacelle anemometer measurements for use in turbine power performance tests, Tech. rep., National Renewable Energy Lab., Golden, CO, USA, <https://www.nrel.gov/docs/fy02osti/32494.pdf> (last access: 19 December 2023), 2002.
- St. Martin, C. M., Lundquist, J. K., Clifton, A., Poulos, G. S., and Schreck, S. J.: Atmospheric turbulence affects wind turbine nacelle transfer functions, *Wind Energ. Sci.*, 2, 295–306, <https://doi.org/10.5194/wes-2-295-2017>, 2017.
- van Beek, M. T., Viré, A., and Andersen, S. J.: Sensitivity and Uncertainty of the FLORIS Model Applied on the Lillgrund Wind Farm, *Energies*, 14, 1293, <https://doi.org/10.3390/en14051293>, 2021.
- van den Broek, M. J., De Tavernier, D., Sanderse, B., and van Wingerden, J.-W.: Adjoint optimisation for wind farm flow control with a free-vortex wake model, *Renew. Energy*, 201, 752–765, 2022.